

TOPICAL REVIEW • OPEN ACCESS

## Efficiency and spectral performance of narrowband organic and perovskite photodetectors: a cross-sectional review

To cite this article: Vincenzo Pecunia 2019 *J. Phys. Mater.* 2 042001

View the [article online](#) for updates and enhancements.

### You may also like

- [Opportunities and challenges of inorganic perovskites in high-performance photodetectors](#)  
Wensi Cai, Haiyun Li, Mengchao Li et al.
- [High-gain and fast-response metal-semiconductor-metal structured organolead halide perovskite photodetectors](#)  
Jie Yang, Tao Yu, Kai Zhu et al.
- [Recent progress of the optoelectronic properties of 2D Ruddlesden-Popper perovskites](#)  
Haizhen Wang, Chen Fang, Hongmei Luo et al.

### Recent citations

- [Engineering Chemical Vapor Deposition for Lead-Free Perovskite-Inspired MA<sub>3</sub>Bi<sub>2</sub>I<sub>9</sub> Self-Powered Photodetectors with High Performance and Stability](#)  
VanHoang Vuong *et al*
- [Assessing the Impact of Defects on Lead-Free Perovskite-Inspired Photovoltaics via Photoinduced Current Transient Spectroscopy](#)  
Vincenzo Pecunia *et al*
- [Organic-based photodetectors for multiband spectral imaging](#)  
Ali Altaqui *et al*



## TOPICAL REVIEW

## OPEN ACCESS

RECEIVED  
27 May 2019REVISED  
14 July 2019ACCEPTED FOR PUBLICATION  
18 July 2019PUBLISHED  
30 August 2019

Original content from this work may be used under the terms of the [Creative Commons Attribution 3.0 licence](#).

Any further distribution of this work must maintain attribution to the author(s) and the title of the work, journal citation and DOI.



# Efficiency and spectral performance of narrowband organic and perovskite photodetectors: a cross-sectional review

Vincenzo Pecunia

Institute of Functional Nano & Soft Materials (FUNSOM), Jiangsu Key Laboratory for Carbon-Based Functional Materials & Devices, Soochow University, 199 Ren'ai Road, Suzhou, 215123, Jiangsu, People's Republic of China

E-mail: [vp293@suda.edu.cn](mailto:vp293@suda.edu.cn)

**Keywords:** narrowband organic photodetectors, narrowband perovskite photodetectors, spectral selectivity, colour sensors, NIR photodetectors

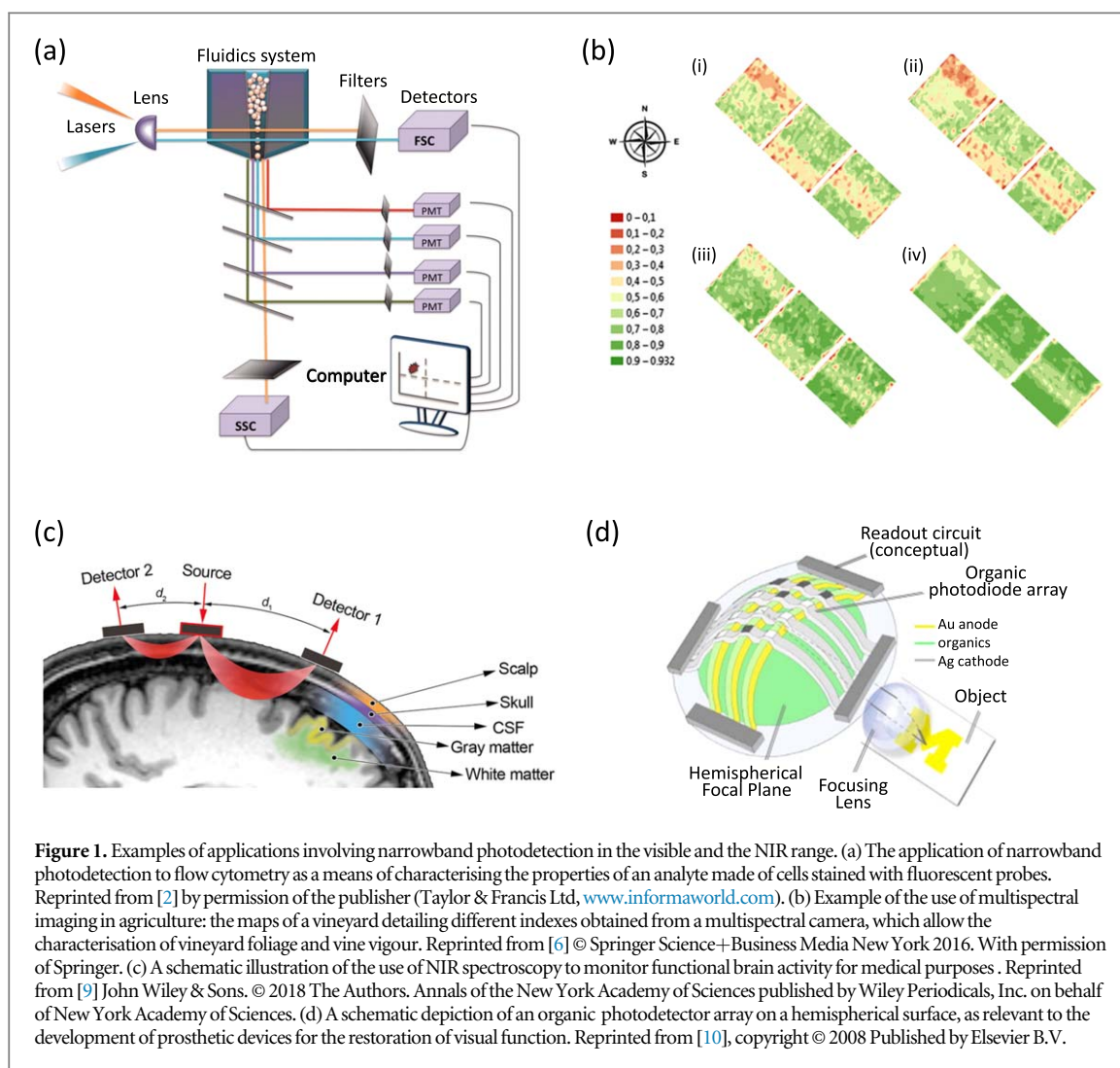
## Abstract

The capability of detecting visible and near infrared light within a narrow wavelength range is in high demand for numerous emerging application areas, including wearable electronics, the Internet of Things, computer vision, artificial vision and biosensing. Organic and perovskite semiconductors possess a set of properties that make them particularly suitable for narrowband photodetection. This has led to rising interest in their use towards such functionality, and has driven remarkable progress in recent years. Through a comparative analysis across an extensive body of literature, this review provides an up-to-date assessment of this rapidly growing research area. The transversal approach adopted here focuses on the identification of: (a) the unifying aspects underlying organic and perovskite narrowband photodetection in the visible and in the near infrared range; and (b) the trends relevant to photoconversion efficiency and spectral width in relation to material, device and processing strategies. A cross-sectional view of organic and perovskite narrowband photodetection is thus delineated, giving fresh insight into the status and prospects of this research area.

## 1. Introduction

Optoelectronic devices capable of detecting light within a narrow spectral range (i.e., narrowband photodetectors) are in ever-growing demand for a wide range of applications. Within the visible range (wavelength  $\lambda \approx 400\text{--}740$  nm), this functionality has been conventionally employed to determine the colour of light with respect to a set of primaries (e.g., three colour bands of  $\approx 100\text{--}150$  nm width), as needed for colorimetry and digital colour photography, for example. This is now highly sought after for a number of growing or emerging areas, e.g., the Internet of Things (IoT), artificial intelligence, computer vision, biosensing [1–3]. Many such emerging areas require tighter performance, e.g., often demanding spectral widths of 100 nm or less [4, 5], and significantly smaller (down to  $\approx 10$  nm) for multispectral and hyperspectral detection/imaging. Over the years, these functional demands have been extended to the near infrared range (NIR,  $\lambda \approx 740\text{--}2000$  nm), which is relevant, e.g., to night vision, navigation aids, astronomy and chemical fingerprinting (for medicine, agriculture, earth sciences, etc) [6–9]. Examples of such applications are shown in figure 1.

Conventional technologies for narrowband photodetection rely on monocrystalline semiconductors with broadband absorption, such as Si and InGaAs. For colour selectivity to be achieved through this approach, the use of input filters is prescriptive. For instance, for multicolour imaging applications the general arrangement involves colour mosaicism via colour filter arrays. While effective, this approach has important downsides, e.g., spatial resolution limitations [11] and colour artifacts [12]. This has led researchers to pursue alternative narrowband strategies within the bounds of conventional semiconductor technologies. These strategies include the use of a dichroic prism that separates light into different spectral components, each being directed to a separate broadband photodetector/imager [13]; the use of patterned metal layers that are integrated within the



photodetector stack and that act as transmission gratings [14]; the use of patterned metal structures that exploit plasmonic effects [15–18].

Organic semiconductors and metal-halide perovskite semiconductors are particularly well-suited for narrowband photodetection in the visible and the near infrared range. First and foremost, their attractiveness arises from the facile tunability of their absorption properties. On one hand, the absorption spectra of organic semiconductors can be tuned nearly at will via molecular design. This enables compounds with either broadband or narrowband absorption, their onsets covering the whole of the visible and the NIR range. On the other hand, while possessing a generally broadband character, metal-halide perovskite semiconductors enable facile tuning of their absorption onset through compositional engineering. In addition to their attractive spectral tunability, organic and perovskite semiconductors typically feature strong absorption (absorption coefficient  $\alpha$  up to  $\approx 10^5 \text{ cm}^{-1}$ ) and high photoconversion efficiency. This allows photodetection to be realised within photoactive layers with a typical thickness of around 100–200 nm, which is ideal for high-resolution imaging applications (cf. thickness in the micrometre range is needed in conventional silicon technology). Finally, both organic and perovskite semiconductors can be deposited at low temperatures ( $< 100 \text{ }^\circ\text{C}$ ) and via solution-based methods (e.g., printing and coating). Therefore, they are particularly attractive for large-area and potentially low-cost manufacturing on flexible plastic substrates, thus pointing to the development of narrowband photodetectors with new functionalities and form factors.

Recent years have witnessed a surge in narrowband photodetector research relying on organic and perovskite semiconductors. Highly efficient and inherently narrowband photodetectors with spectral widths of about 100 nm have become possible. Additionally, effective strategies have been developed so as to harness broadband organics and perovskites in narrowband photodetectors with spectral widths down to 10 nm. This review is motivated by the need for an up-to-date assessment of this rapidly growing research area, particularly with respect to photoconversion efficiency and spectral width, which are central to narrowband functionality. While recent reviews on organic and perovskite narrowband photodetection have captured a broad view of the area [19–21], the present article pursues a focused approach aiming at the identification of the general trends associated with photoconversion efficiency and spectral width. Indeed, the growing body of literature poses

significant challenges to attempts at comparing photoconversion efficiency and spectral width figures achieved with different materials and device solutions, especially due to the inherently heterogeneous nature of the reported performance data. Consequently, a cross-sectional analysis of the literature is in order so as to put recent developments in context and to reassess the potential of organic and perovskite narrowband photodetectors.

## 2. Photoconversion efficiency and spectral performance

The key functional requirement of organic and perovskite narrowband photodetectors is to convert photons within a specified wavelength range efficiently into photocurrent. Consequently, the efficiency of this process (photoconversion) and its spectral performance constitute two characteristic aspects of narrowband photodetector performance, and are therefore taken as the focus of this review.

The photoconversion efficiency of a narrowband photodetector can be expressed in terms of its external quantum efficiency (EQE). This is defined as the ratio between the number  $N_e$  of electron–hole pairs collected at its electrodes, and the number of photons  $N_{ph}$  incident on the photodetector (per unit time):  $EQE = N_e / N_{ph}$ . In terms of device-level quantities, the EQE relates to the ratio between the photocurrent  $i_{ph}$  and the incident optical power  $P_{opt}$ :  $EQE = (hc) / (q\lambda) \cdot i_{ph} / P_{opt}$ , where  $h$  is the Planck constant,  $\lambda$  and  $c$  are the wavelength and the speed of the incident light in free space, and  $q$  is the elementary charge. In fact, the photoconversion process can also be described in terms of the responsivity, which is an equivalent device-level metric:  $R = i_{ph} / P_{opt}$ .

Both the EQE and responsivity are aggregate measures of the efficiency of the manifold processes underlying photoconversion. Indeed, photoconversion requires the absorption of incident photons (which occurs with efficiency  $\eta_{abs}$ ), the generation of photocarriers (with efficiency  $\eta_{gen}$ ) as a result of photon absorption, and the transport of photocarriers to the electrodes (with efficiency  $\eta_{tr}$ ), at which they are finally extracted (with efficiency  $\eta_{extr}$ ). Due to the wavelength dependence of some of these processes, the EQE and responsivity are also functions of wavelength, a property that is key to narrowband photodetection.

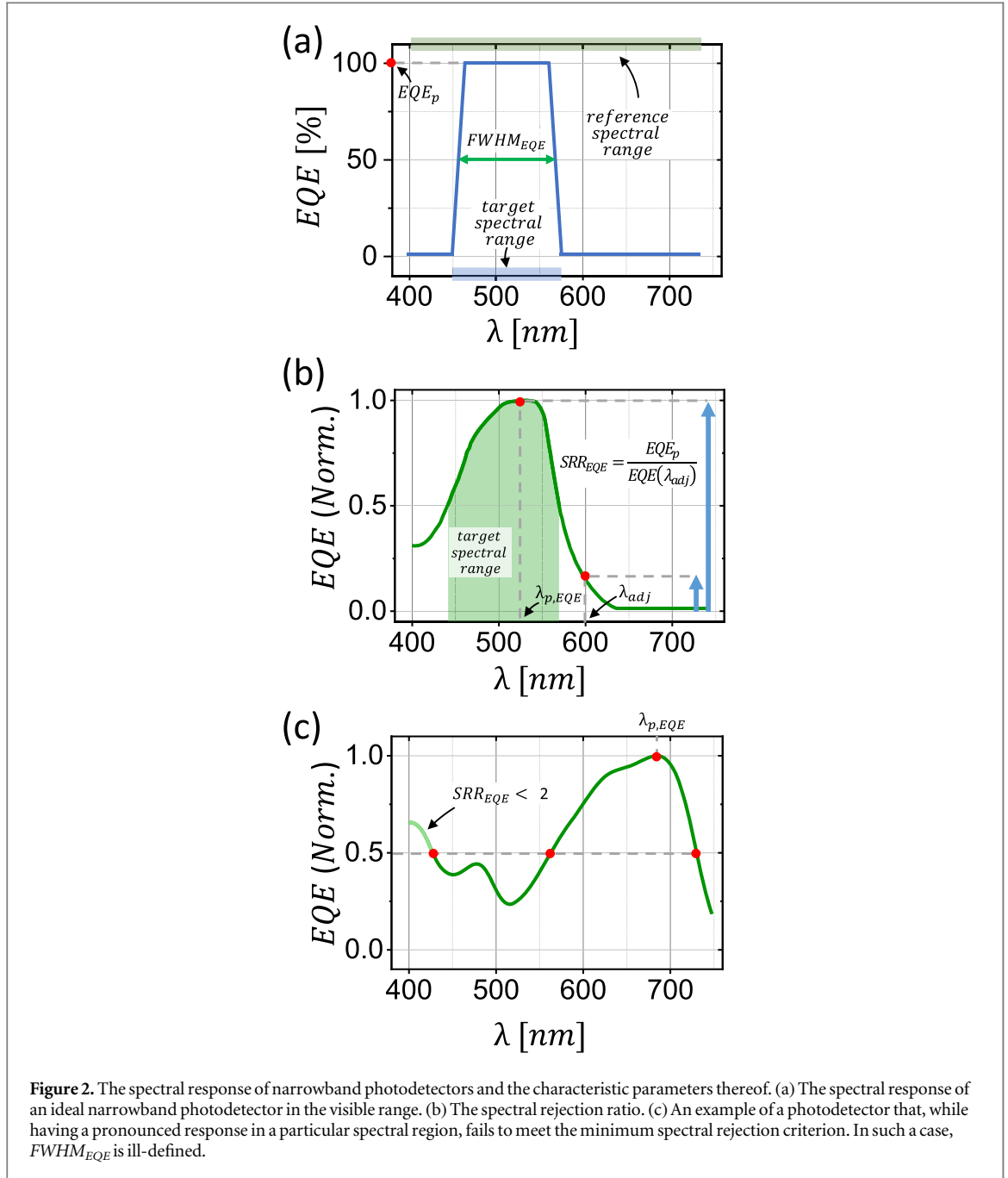
The EQE of a photodetector is typically smaller than unity due to the finite losses in the processes underlying photoconversion (primary photocurrent operation). In some device configurations (see section 3), however, it is possible to extract a rather large number of photocarriers per absorbed photon (secondary photocurrent operation). In such cases, the number of extracted photocarriers per absorbed photon is also referred to as photoconductive gain  $G$ .

The wavelength range within which a narrowband photodetector has significant responsivity is referred to as the *responsivity passband*. Within the responsivity passband one can identify a maximum responsivity  $R_p$  at a wavelength  $\lambda_{p,R}$ . Additionally, the extent of the responsivity passband is referred to as the *responsivity width*, and is most typically expressed in terms of the full width at half-maximum,  $FWHM_R$ . *Mutatis mutandis*, one can define the peak EQE ( $EQE_p$ ), the EQE peak wavelength ( $\lambda_{p,EQE}$ ), and the corresponding EQE width,  $FWHM_{EQE}$  (see figure 2(a)).

An ideal narrowband photodetector should possess a passband that precisely overlaps the spectral range that is meant to be detected (*target spectral range*, see figure 2(a)). At the same time, it should possess negligible responsivity outside the target spectral range, within the bounds relevant to the application at hand (*reference spectral range*, see figure 2(a)). For instance, a photodetector targeting green detection for digital photography should have a responsivity passband extending over  $\approx 500$ – $600$  nm, and its responsivity should be negligible for other wavelengths in the visible range ( $\approx 400$ – $740$  nm being the reference range for colour detection).

While a passband larger than the target spectral region is widely understood as being detrimental to achieving good spectral selectivity, it should also be appreciated that a passband much smaller than the target spectral range is also undesired. Indeed, if the latter case holds, negligible photoresponse would be obtained for some of the wavelengths of interest. It is therefore apparent that the ideal responsivity width is determined by the application at hand, and is to be minimised only within the corresponding bounds. For instance, spectral widths of 100–150 nm are sufficient for digital photography (cf. CIE colour matching functions and prototypical spectral response of commercial silicon colour sensors), while widths in the region of 75–100 nm are needed for illuminant-independent colour determination for computer vision [4, 5]. Multispectral and hyperspectral imaging instead typically require ultranarrowband performance, i.e., widths  $< 50$  nm (of course, unsuitable for tricolour digital photography).

In addition to the responsivity/EQE width, the narrowband capability of a photodetector is also to be quantified in relation to how its response within the target spectral range compares to the response outside it (*spectral rejection*). One measure that is often used to appraise this property is the spectral rejection ratio  $SRR_R$ , defined as:



$$SRR_R(\lambda_{peak}, \lambda_{adj}) = \frac{R(\lambda_{p,R})}{R(\lambda_{adj})}$$

where  $\lambda_{adj}$  is a particular wavelength outside the target spectral range (within the bounds of the reference range). *Mutatis mutandis*, an equivalent quantity can be defined in reference to the EQE ( $SRR_{EQE}$ ) (see figure 2(b)). Good spectral rejection is ensured by a large spectral rejection ratio for all wavelengths  $\lambda_{adj}$ . It is useful to note that for an  $SRR_R < 2$  ( $SRR_{EQE} < 2$ ) at any  $\lambda_{adj}$ , the  $FWHM_R$  ( $FWHM_{EQE}$ ) is ill-defined, even in the presence of a clear responsivity (EQE) band over the target spectral region (figure 2(c)). In view of this, we shall refer to the condition  $SRR_{R/EQE} > 2$  as the minimum spectral rejection criterion for a narrowband photodetector.

### 3. Device architectures

Both organic and perovskite photodetectors deliver narrowband functionality through the same types of device architectures, photoconductors and photodiodes. The key aspects of each are summarised in the following.

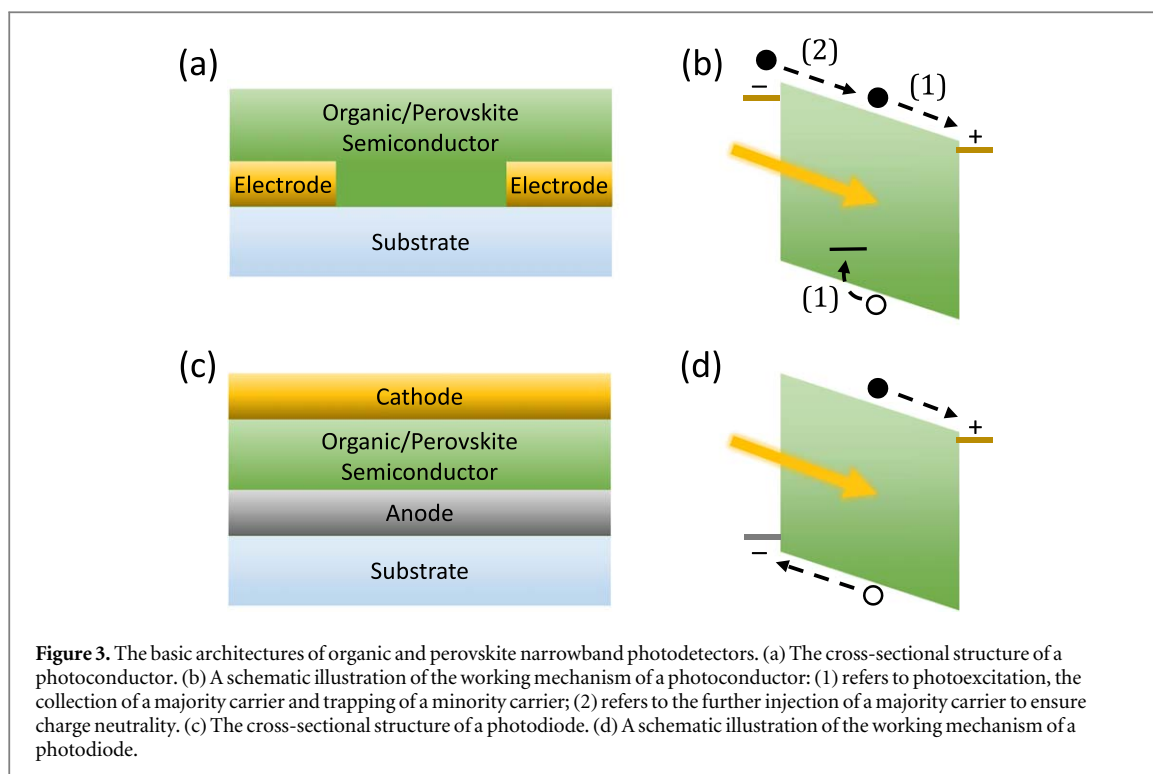


**Figure 3.** The basic architectures of organic and perovskite narrowband photodetectors. (a) The cross-sectional structure of a photoconductor. (b) A schematic illustration of the working mechanism of a photoconductor: (1) refers to photoexcitation, the collection of a majority carrier and trapping of a minority carrier; (2) refers to the further injection of a majority carrier to ensure charge neutrality. (c) The cross-sectional structure of a photodiode. (d) A schematic illustration of the working mechanism of a photodiode.

### 3.1. Organic/perovskite photoconductors

An organic/perovskite photoconductor is realised by placing the photoactive material between two Ohmic contacts. This is customarily implemented in a gap cell structure (figure 3(a)). For instance, Lim *et al* implemented one such device with a film made of an anthracene derivative placed between gold electrodes [27], while Saidaminov *et al* utilised a polycrystalline film of MAPbI<sub>3</sub> placed between ITO electrodes [28]. Within a photoconductor, as the amount of light absorbed in the photoactive material increases, a reduction of the device resistance is observed. The photocurrent flowing through the device is associated not only with carriers resulting from direct absorption (primary photocurrent), but also with carriers injected from the electrodes upon light absorption so as to maintain charge neutrality (secondary photocurrent) (figure 3(b)). The latter contribution is proportional to the ratio between carrier lifetime and transit time—this ratio being equal to the photoconductive gain  $G$  of the device (section 2). The photoconductive gain can be rather large for particular material and device configurations, in which case the secondary photocurrent is dominant. In such operating conditions, the number of carriers flowing under illumination per absorbed photon can be much larger than unity (i.e.,  $\text{EQE} \gg 1$ ). This is a direct result of this particular device configuration, and does not constitute an indication of the superior optoelectronic properties of the photoactive material employed.

### 3.2. Organic/perovskite photodiodes

An organic/perovskite photodiode consists of a photoactive layer placed between two asymmetric contacts, typically arranged in a sandwich structure (figure 3(c)). This configuration is the most explored in the literature, and numerous examples are presented in section 6. In particular, one of the contacts (the anode) is intended to collect photogenerated holes, while the other (the cathode) is for electrons (figure 3(d)). The energetics of the contacts with respect to each other and to the energy levels of the photoactive material results in a rectifying current–voltage characteristic. In particular, photodetection in a photodiode is typically carried out with negative voltages applied to the anode with respect to the cathode (reverse bias), as in this bias region the photocurrent is set against a rather small dark current (i.e., current under no illumination).

In contrast to photoconductors, photodiodes most typically operate in primary photocurrent mode, i.e., at best only one electron–hole pair is collected per absorbed photon (figure 3(d)). Under appropriate conditions, however, a photodiode can also manifest a photoconductive gain [29]. This typically relies on the incorporation of trap states for one particular type of carrier (referred to as the minority carrier in this context). For example, Miao *et al* and Wang *et al* relied on minute amounts of fullerenes to introduce a trap state within a hole-conducting polymer (P3HT) [30–32], while Shen *et al* employed inorganic quantum dots to achieve a similar effect within an organic donor–acceptor blend [33, 34]. Under illumination and sufficiently strong bias, the injection barrier for majority carriers (i.e., the more mobile carrier in the photoactive material) may be thinned to the point at which majority carrier tunnelling into the photoactive material occurs [29]. This determines a

secondary photocurrent, which, just as in the case of a photoconductor, can be associated with a particularly large gain (see section 6.4 for a discussion on literature implementations).

## 4. Key material and optoelectronic properties of organic and perovskite semiconductors

Prior to delving into the different narrowband strategies (section 5) and presenting our cross-sectional analysis of narrowband device performance (section 6), here we provide an overview of the essential material and optoelectronic properties of organic and perovskite semiconductors relevant to narrowband photodetection. In keeping with the spirit of this review, emphasis is placed on the shared traits and differences of these two semiconductor families. After presenting the key aspects concerning photon absorption and photoexcitation, we discuss the specifics of each of these semiconductor families.

### 4.1. Generalities on absorption and photoexcitation

In reference to their absorption properties, organic and perovskite semiconductors can be divided into narrowband absorbers, broadband absorbers and transparent compounds—all of which find use in narrowband photodetectors. Due to their semiconducting nature, these compounds all feature an absorption onset at some wavelength  $\lambda_{onset}$  (e.g., see figures 4(b), (c)), which relates to the optical bandgap  $E_g^{(opt)} = hc/\lambda_{onset}$ . Both narrowband and broadband absorbers have their onsets within the reference spectral range (section 2). This is in contrast to the case of transparent compounds, for which  $\lambda_{onset}$  falls outside the reference range (at shorter wavelengths). Narrowband absorbers possess a single, dominant absorption band within the reference spectral range, hence it becomes possible to define the FWHM of their absorption coefficient ( $FWHM_{\alpha}$ ) (e.g., see figure 4(b)). Broadband absorbers, instead, absorb significantly for all wavelengths below their onsets (e.g., see figure 4(b)). The use of each of these types of compounds for narrowband photodetection is detailed in section 5. At this stage it suffices to note that narrowband absorbers constitute a particularly attractive class of compounds for narrowband photodetection, as they provide a direct route to narrowband photodetection (section 5.1).

The nature of the primary photoexcitations in organic and perovskite semiconductors is a crucial aspect of the operation and performance of the resulting narrowband photodetectors. In particular, an essential distinction relates to whether photon absorption delivers quasi-free electrons and holes, or, instead, excitons. If the generation of quasi-free photocarriers is possible, the efficiency of the photoconversion process depends significantly on the transport of photocarriers to the electrodes, and on their extraction at the associated interfaces. In excitonic materials instead an energy barrier (i.e., the exciton binding energy) must be overcome for quasi-free carriers to be generated after light absorption. This, in turn, requires the engineering of the photoactive material so as to enable efficient exciton dissociation into quasi-free photocarriers. Ensuing photocarrier generation through exciton dissociation, efficient carrier transport and extraction at the electrodes are also needed for efficient photoconversion.

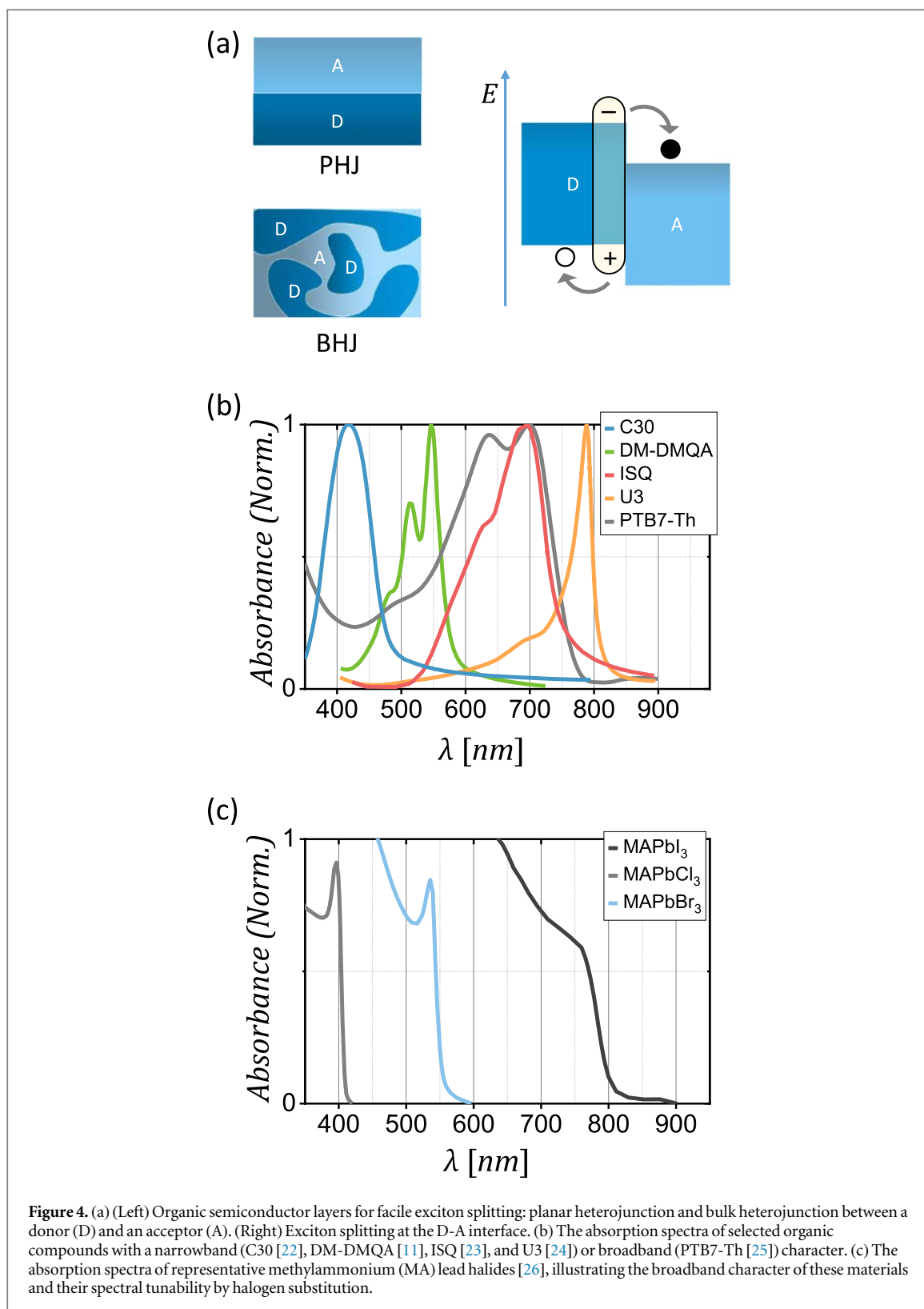
A general feature of organic and perovskite semiconductors is that both families comprise a large number of compounds with particularly strong absorption in the visible and/or NIR range. Indeed, the in-band absorption coefficient of many of these compounds is greater than  $10^5 \text{ cm}^{-1}$  [35, 36]. Therefore, films only a few hundred nanometres in thickness can absorb most in-band incident light. This is particularly attractive for high-performance narrowband photodetection.

### 4.2. Organic semiconductors

Organic semiconductors constitute a broad family of semiconducting materials, which come in the form of  $\pi$ -conjugated small molecules and polymers. Small molecules may present varied absorption properties—narrowband, broadband and transparent (e.g., through the visible range)—while polymers are generally broadband absorbers. This different character is closely linked to the conformational disorder typical of polymeric systems [37, 38].

Organic semiconductors have an excitonic character (exciton binding energy  $\gg$  thermal energy at room temperature) [39], which results in their generally low photogeneration efficiency in single-component form. Hence, their use in narrowband photodetectors most often relies on a pair of compounds forming blends (bulk heterojunctions, BHJs) or bilayers (planar heterojunctions, PHJs), which synergistically allow exciton dissociation and quasi-free carrier generation (figure 4(a)). The compound (in the pair) that contributes an electron via interfacial exciton dissociation is referred to as the donor (D), while the other is the acceptor (A). Both are essential for the realisation of narrowband photodetectors.

In addition to its fundamental absorption onset, a donor can deliver a lower-energy absorption band when forming an interface with an acceptor (e.g., as in a BHJ). This lower-energy absorption band relates to the charge transfer (CT) exciton state that can be formed at such interfaces [40, 41]. Being at longer wavelengths than the



fundamental absorption onsets of the component materials, this feature is particularly attractive in some narrowband device configurations aimed at NIR-selective photodetection [42, 43].

A further aspect that is particularly important for the use of organic semiconductors in photodetectors concerns their charge transport properties. Organic semiconductors can be generally regarded as low-mobility materials. Indeed, compounds typically employed in narrowband photodetectors to date feature mobility values in the  $10^{-5}$ – $10^{-2}$   $\text{cm}^2 \text{V}^{-1} \text{s}^{-1}$  range. Mobility is a key determinant of the photocarrier drift length (distance travelled prior to undergoing recombination), which in turn affects the overall photoconversion efficiency. In spite of the comparatively low mobility, the charge transport properties of organic semiconductors may not pose

a limit to the overall photoconversion efficiency, thanks to the considerably low thickness of the photoactive layers employed (see discussion of absorption properties in section 4.1). In addition, it is noteworthy that their low-mobility character is key to their use and performance for some narrowband photodetection strategies (see section 5.3).

Small-molecule semiconductors with narrowband absorption properties have played a key role in the development of organic narrowband photodetectors (see section 5.1). A significant number of them are drawn or derived from compounds originally developed as industrial colourants, laser dyes, or fluorescent probes—e.g., blue-absorbing coumarins [22, 44–47], green-absorbing rhodamines [44, 45, 48–51] and quinacridones [11, 47, 52–63], green- and red-absorbing phthalocyanine metal/metalloid complexes and derivatives [11, 44, 45, 47, 49, 54–56, 58, 61, 64–70], and green-, red-, and NIR-absorbing squaraines [23, 71–73] (figure 4(b)). It is noteworthy that some narrowband-absorbing small molecules are able to form aggregates (J- and H-aggregates) featuring particularly narrow and intense absorption bands ( $FWHM_{\alpha} < 20$  nm,  $\alpha$  up to  $10^6$  cm<sup>-1</sup>), a property that is very attractive for narrowband photodetection [24, 74–79].

Among small-molecule semiconductors, fullerenes have been central to the development of organic narrowband photodetectors, in view of their long-standing role as acceptor moieties par excellence. Their outstanding electron-accepting properties in BHJs and PHJs (in combination with polymeric and small-molecule donors alike) have led to their widespread use in all types of narrowband photodetector configurations [19, 30, 31, 80–85]. However, their broad absorption tail through the visible has been problematic in some configurations (see section 6.3), and this has recently prompted the development of alternative small-molecule acceptors with narrowband absorption [11, 57–61] or with diverse onsets [42, 86–88].

Polymers have also been widely employed in the photoactive layers of organic narrowband photodetectors. Their use relates to either their broadband absorption or their transparency through the visible and NIR range. In either case, they have been utilised as donors (within donor-acceptor BHJs or PHJs) or as hole transporting semiconductors (if used in single-component form). Depending on the composition, their absorption onset can fall in different spectral regions—for instance, in the blue (as in some polyfluorene-based polymers) [49–51, 84, 86, 89–95], in the red (as in some polythiophenes) [25, 30–33, 42, 80–82, 84, 96, 97], and in the far red/NIR (as in a number of so-called D-A polymers) [25, 32, 42, 98–100].

### 4.3. Metal-halide perovskites

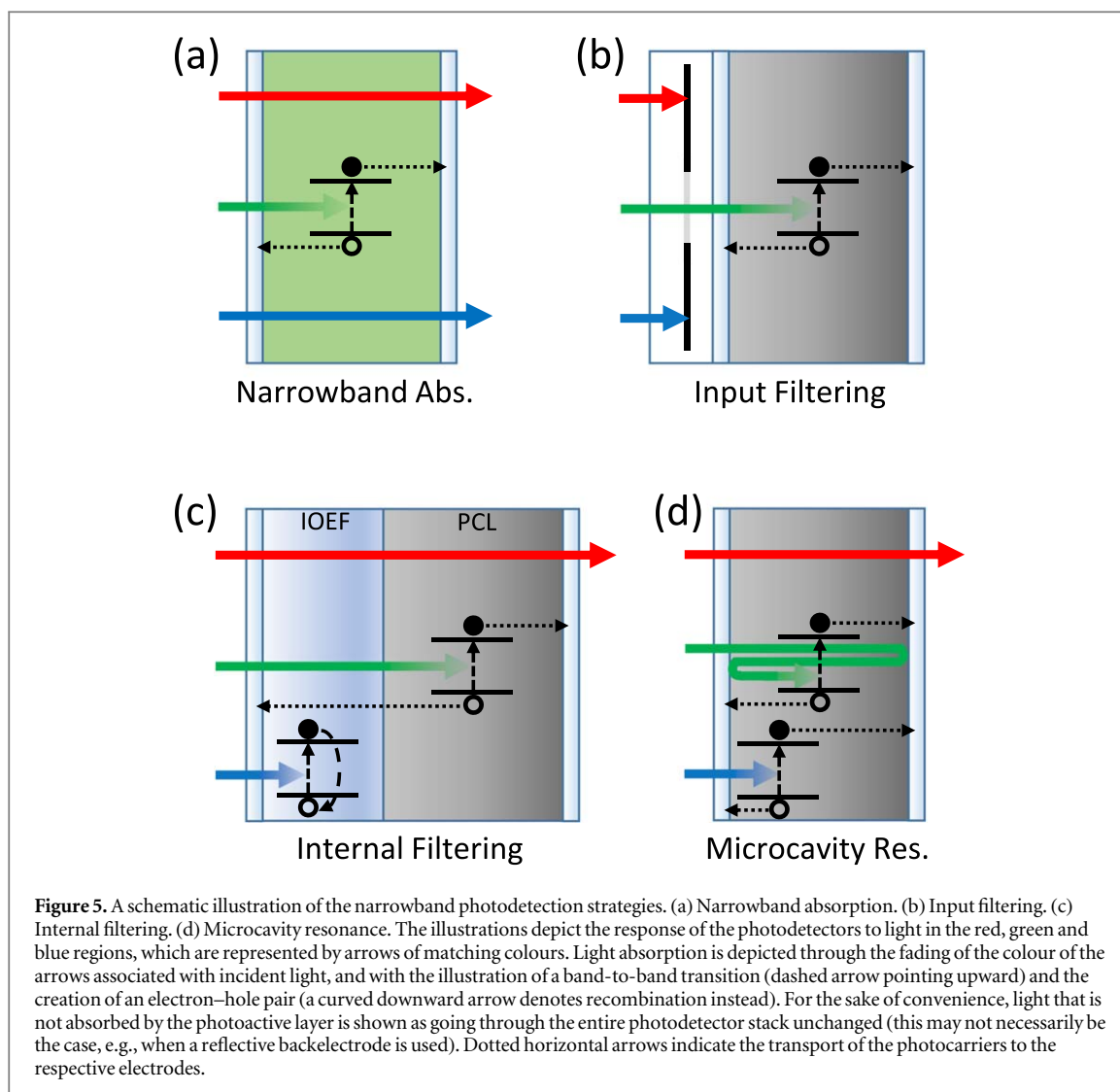
Metal-halide perovskites constitute a large family of semiconductors, which, in their mainstream embodiments, have the formula  $AMX_3$ , A being a monovalent cation (organic, inorganic, or a mixture of both), M being lead, and X a halogen. For the sake of compactness, in the following we shall use the word perovskite to refer to these mainstream embodiments, unless noted otherwise.

Perovskites for narrowband photodetection have been reported both in the form of macroscopic single crystals as well as polycrystalline thin films. While the former present crystalline order throughout their volume, the latter consist of small crystalline regions (grains) that terminate abruptly at the interface (grain boundary) with other crystalline regions.

The absorption onset of perovskites can be tuned by varying the electronegativity of the halide, either through substitution or mixing. For the sake of illustration, the absorption onsets of representative lead-halide perovskites are shown in figure 4(c). In the case of mixed halides, a continuum of bandgap values is achievable by fine tuning their mixing ratio. For instance,  $MAPbBr_{3-x}Cl_x$ ,  $0 < x < 3$ , leads to absorption onsets ranging from blue to green, while  $MAPbI_{3-x}Br_x$ ,  $0 < x < 3$ , leads to absorption onsets ranging from green to NIR (MA being the short form of  $CH_3NH_3$ ). Additionally, mainstream perovskites feature a rather sharp absorption onset (Urbach energy in the region of 15 meV) [36, 101]. Both spectral tunability and onset sharpness are particularly attractive for narrowband photodetection (see section 5).

As far as the nature of their primary photoexcitations, mainstream perovskites do present an excitonic absorption edge, yet their exciton binding energy is rather small. For instance, this energy is of a few meV in  $MAPbI_3$  [102], in which case, for practical effects, absorption at room temperature (as relevant to narrowband photodetector applications) results in quasi-free electron–hole pairs at room temperature [103]. For mainstream perovskites with increasing halide electronegativity, however, the exciton binding energy increases to a few tens of meV (e.g., 21 meV in  $MAPbBr_3$  and 50 meV  $MAPbCl_3$ ) [104].

Lead-halide perovskites have been generally reported to possess good charge transport properties. Mobility values extracted from single crystals are of the order of  $1$ – $100$  cm<sup>2</sup> V<sup>-1</sup> s<sup>-1</sup>. However, mobility is reduced in polycrystalline films, with values in the  $0.05$ – $0.2$  cm<sup>2</sup> V<sup>-1</sup> s<sup>-1</sup> range. Additionally, films with large grain sizes have been reported to produce larger mobility values [105]. Notwithstanding the comparatively limited mobility, particularly long carrier drift lengths (e.g., from several micrometres to several millimetres) [106, 107] in moderate fields have been reported in perovskites, which is key to achieving high transport efficiency in photodetectors.



While featuring attractive optoelectronic properties, hybrid lead-halide perovskite materials have been found to be significantly prone to instability and degradation effects. On one hand, hysteretic device  $I$ – $V$  characteristics are often observed. On the other, lead-halide perovskites undergo degradation/decomposition in ambient conditions [108]. Their degradation is compounded by extrinsic factors/stimuli such as moisture, thermal stress, electrical stress and light [108, 109]. While significant effort has been put forth to address these effects, instability and degradation still constitute a significant challenge.

## 5. Strategies for narrowband photodetection with organic and perovskite semiconductors

Several strategies have been explored to date to achieve narrowband photodetection with organic and perovskite semiconductors. In spite of the differences between these two material families, the significant overlap of their properties allows a unified discussion of the relevant narrowband strategies, which is presented in this section.

### 5.1. Narrowband absorption

The most direct approach to narrowband photodetection consists of having a narrowband absorber as the photoactive layer. In such a case, only photons within the absorption passband of the photoactive layer are absorbed and deliver significant photocurrent (figure 5(a)). Therefore, the success of this strategy closely depends on using a narrowband absorber whose absorption passband matches the target spectral range. We shall refer to the resulting photodetectors as narrowband-absorption-type (NBA-type in short form).

This approach is readily applicable to a wide number of organic semiconductors capable of narrowband absorption. In contrast, perovskite semiconductors do not lend themselves to this strategy due to their generally broadband absorption character.

NBA photodetectors are particularly attractive for multicolour and multispectral imaging applications. Indeed, stacked NBA-type photodetectors responsive in adjacent spectral regions, and with transparent electrodes would allow multicolour/multispectral detection at the same location within an imager [54, 56, 110–112]. Moving away from colour mosaicism (section 1), NBA-type stacking thus holds the promise of overcoming the limitations of conventional imaging technologies [13]. It is important to note that this advantage arises from the nonfiltering nature of the NBA approach, i.e., from its little to negligible light absorption outside the responsivity passband, and from its capability to function with transparent electrodes. As will become clear in the following, this property is unique to the NBA strategy, as all other approaches developed to date involve some filtering mechanism, which alters the spectral content of the light outside the responsivity passband.

## 5.2. Input optical filtering

Input optical filtering (InpF in short form) is a means of achieving narrowband photodetection by combining a photoactive material capable of broadband absorption with an external optical filter (figure 5(b)). The latter is used to dissipate photons outside the target spectral range, while allowing all others to reach the photoactive material. This strategy places the spectral burden of narrowband photodetection on the external filter, while great flexibility is allowed in regard to the absorption properties of the photoactive material. As many organic and perovskite semiconductors are capable of broadband absorption, this strategy is readily applicable to both semiconductor families. In fact, this strategy originates from (and has long been applied to) conventional narrowband photodetection technologies (e.g., c-Si-based), for which it constitutes the mainstream approach.

Within this approach to narrowband photodetection, it is particularly noteworthy that organic and perovskite semiconductors can be used not only as photoactive materials, but also as filter materials. This is enabled by the facile tunability of their absorption properties [83, 113]. A particular implementation of this strategy involves using a filter made of a broadband photodetector with absorption (and responsivity) onset at a shorter wavelength than that of the photodetector at hand (input optical filtering with stacking) [113]. In principle, stacking multiple broadband photodetectors along similar lines has the merit of delivering narrowband devices covering multiple adjacent spectral bands (e.g., as needed for RGB colour detection).

## 5.3. Internal filtering

Internal filtering relies on a broadband photoactive layer featuring an inherent optoelectronic mechanism that suppresses the photoresponse outside the target spectral range. In particular, while a slice of the photoactive layer actively contributes to photoconversion (photoconversion layer, PCL), the remainder (typically placed next to photodetector input surface) serves the purpose of dissipating photons outside the target spectral range (internal optoelectronic filter, IOEF) (figure 5(c)). The spectral distribution of the photons reaching the photoconversion volume is thus narrowed, resulting in a narrowband photoresponse. Internal filtering can be realised in a number of ways, the salient features of which are presented in the following and summarised in table 1.

Organic semiconductors can provide internal optoelectronic filtering through exciton and/or photocarrier recombination. Considering a single-component photoactive layer with a unipolar transport character, if its thickness is much larger than its exciton diffusion length, severe exciton recombination is expected for light absorbed in its bulk. In particular, if the thickness of the layer is greater than its in-band absorption depth, then in-band photons are fully absorbed in the bulk yet do not lead to significant photocurrent (due to exciton recombination), thus realising an optoelectronic filtering effect. Additionally, the photocarriers generated by exciton dissociation at the interface with the input electrode undergo severe recombination (due to the unipolar transport character of the semiconductor), thus yielding negligible photocurrent. Consequently, the single-component photoactive layer delivers a photoresponse peaking nearby its absorption onset, as determined by the optoelectronic filtering effect just described, which confines efficient photogeneration to the region nearby the back electrode [73, 96]. We shall refer to this configuration as single-component internal filtering (IntF-1 in short form). It is noteworthy that the IntF-1 working principle also applies to photoactive layers made of blends of two different organic semiconductors, provided that both feature the same type of unipolar transport, and that their interfaces do not favour exciton dissociation. If these conditions hold, such a photoactive layer behaves as an *effective* unipolar single-component semiconductor, hence allowing narrowband photodetection in the IntF-1 mode. Finally, if minute amounts of minority carrier traps are incorporated into the single-component (either per se or de facto) photoactive layer, IntF-1 may take place with a concurrent gain mechanism (IntF-1x in short form) (cf. section 3.2) [25, 30–32]. The latter case is often referred to as charge injection narrowing in the literature [29].

Another possible configuration of internally filtered organic narrowband photodetectors involves having the internal optoelectronic filter and the photoconversion layer made of different materials, which are placed next to each other so as to form a planar heterojunction (IOEF|PCL in short form). For the sake of illustration, this

**Table 1.** Different configurations of internally filtered photodetectors with narrowband functionality.

Internally filtered configurations					
Configuration	IOEF-PCL planar heterojunction (IOEF PCL)		Single component (IntF-1)	Charge collection narrowing (CCN) and dual-absorption CCN (DA-CCN)	
Material class	Organic		Organic	Organic/perovskite/perovskite:organic	
Basic structure	Two distinct layers for optoelectronic filtering and photoconversion		One organic single-component layer with broadband absorption and unipolar transport	One layer (organic D:A, or perovskite, or perovskite:organic) with broadband absorption and balanced ambipolar transport	
Filtering mechanism	Absorption and exciton annihilation		Absorption and exciton annihilation/charge recombination	Absorption and charge recombination	
IOEF	Donor (acceptor) in D A OPD	Transport layer	Input interface and bulk of photoactive layer		Surface region of photoactive layer
PCL	Acceptor (donor) in D A OPD	D A or D:A	Back interface of photoactive layer		Bulk of photoactive layer
Passband	Spectral region where absorption of IOEF and PCL do not overlap		Vicinity of absorption onset of photoactive material	Vicinity of absorption onset of photoactive material (CCN)	Spectral region of intermediate plateau absorption (DA-CCN)
Gain	—		Via minority trap (IntF-1x)	Via unipolar trap (CCNx)	—

configuration can be implemented with a D-A planar heterojunction in which, e.g., the donor layer is closest to the photodetector input surface, and is much thicker than its exciton diffusion length and its in-band absorption depth. Photons absorbed in the bulk of the donor layer are then dissipated (via exciton recombination), thus preventing them from delivering any photocurrent, and also from reaching the photoconversion volume at the interface with the acceptor. This leads to appreciable photoresponse only at wavelengths where the absorption spectra of the donor and acceptor do not overlap significantly [68, 84]. Alternatively, the IOEF|PCL configuration can be attained by having a transport layer function as an internal optoelectronic filter [69, 73, 114].

Apart from configurations relying on exciton recombination, it is also possible to achieve internal optoelectronic filtering with organic semiconductors by exclusively relying on photocarrier recombination. This mechanism is widely referred to as charge collection narrowing (CCN), and generally involves a photoactive layer in the form of a D-A bulk heterojunction which is significantly thicker (typically, in the micrometre range) than its in-band absorption depth. Note that such a photoactive layer, in contrast to the IntF-1 case, is capable of ambipolar transport and efficient exciton dissociation. Due to the large thickness of the photoactive layer, photocarriers generated by in-band photons have significantly imbalanced transit times. This leads to appreciable photocarrier recombination (enhanced by space-charge effects), which suppresses the contribution of in-band photons to the photodetector response. This then leads to an ultranarrow photoresponse around the absorption onset of the photoactive layer. Indeed, photocarriers generated in such a spectral region have a more balanced transit time, hence recombination losses are not as severe [33, 34, 73, 85, 86, 98, 115]. By incorporation of carrier traps in the photoactive material, CCN operation can also be combined with a gain mechanism (CCNx in short form) [33, 34].

Internal filtering fully relying on photocarrier recombination has also been explored with perovskite photodetectors. In this case, recombination occurs via surface and/or bulk states. This approach is also referred to as charge collection narrowing in the context of perovskites, and works along the same lines as in the organic case [28, 116–119]. It is noteworthy that when using a perovskite-only photoactive material, a much thicker layer (from tens of micrometres to millimetres) is required compared to the organic case, in view of the significantly longer photocarrier drift length of perovskites (see section 4.1). However, if the perovskite is blended with an organic component, the resulting optoelectronic properties may be conditioned in such a way that sub-micrometre photoactive layers can be employed [117]. It is noteworthy that perovskite-organic blends allow a variation on the basic CCN-type devices (common to organic-only and perovskite-only works) featuring a photoactive layer with generally high absorption below the fundamental onset  $\lambda_{onset}$ . Indeed, perovskite-organic blends can be engineered to have an absorption spectrum featuring an intermediate plateau between the fundamental onset and the high-absorption region. By suitably sizing the photoactive layer thickness, it then becomes possible to achieve narrowband photodetection with the passband falling over the spectral region of the intermediate absorption plateau (dual-absorption CCN, DA-CCN) [117].

#### 5.4. Microcavity resonance

If reflective electrodes are used within a sandwich-type device structure, constructive interference of the optical field occurs when the round-trip optical path length is an integer multiple of the wavelength (resonance condition). This turns the photodetector into a resonant microcavity ( $\mu$ C in short form), and allows the enhancement of its photoresponse at its resonance wavelengths. This is relevant to spectral regions where the photoactive material absorbs weakly, so as to ensure minimal optical losses and thus allow constructive interference. For instance, resonances can be established at wavelengths approaching the absorption onset. Additionally, this approach has been successfully implemented to enhance the photoresponse within the CT absorption band of a D-A BHJ. Interestingly, while a number of works have explored this approach with organic semiconductors, no report has emerged to date on its application to perovskites.

Finally, it is important to note that this method is unable to suppress the nonresonant photoresponse within the absorption band of the photoactive material. This implies that a microcavity-type device requires input optical filtering to achieve narrowband photoresponse within the full reference spectral range.

## 6. Cross-sectional performance analysis

Considering the large and growing body of literature on organic and perovskite narrowband photodetectors, a cross-sectional analysis is key to being able to capture performance trends, and their relationship to material and device aspects. Efficient photoconversion and a suitably narrow passband are the two essential features demanded of a high-performance narrowband photodetector. Consequently, we shall focus on EQE and spectral width as the primary performance metrics throughout our analysis. The values of these metrics from the relevant literature are listed in tables 2–7. In the following, we examine these metrics from multiple angles: materials (section 6.1); narrowband

**Table 2.** Organic NBA narrowband photodetectors from the literature. The entries are grouped into blue-, green-, red- and NIR-responsive photodetectors, and are listed in chronological order within each of these groups; † with stacking, ‡ NBA with gain, \*  $FWHM_{EQE}$  is ill-defined over the visible, as  $SRR_{EQE} < 2$ . § is strongly dependent on optical power. || D is reported as being one of the donors also explored by Bulliard *et al* [120]. ¶ while the peak wavelength is out of the spectral range taken here as red, the photoresponse of this particular implementation is predominantly in the red. Process: sol. (solution-based); vac. (vacuum-based). S in the Architecture column denotes the photoactive layer.

Organic NBA photodetectors						
Article	Photoactive layer	Process	Architecture	$EQE_p$ %	$\lambda_p$ /(colour) nm/—	FWHM nm
Kudo 1981 [48]	ZnO MC <sub>60</sub>  RB	Vac.	ITO S Al	6	470	116
Aihara 2003 [44, 45]	C6:PHPPS	Sol.	ITO S Al	<0.7	420	>98
Antognazza 2007 [97]	MeLPPP	Sol.	ITO S Al	≈0.1	453	51
Seo 2007 [54]	Co-TPP Alq <sub>3</sub>	Vac.	ITO S NTCDA ITO	8	419	35
Fukuda 2009 [49]	F8BT	Sol.	ITO S LiF Al	$8.8 \cdot 10^{-2}$	449	>110
Fukuda 2009 [94]	F8BT	Sol.	ITO S LiF Al	$2.2 \cdot 10^{-1}$	(blue)	n.a.
Fukuda 2010 [93]	DMTP-S:F8BT	Sol.	ITO S LiF Al	1.7	470	120
Kobayashi 2010 [90]	NMe <sub>2</sub> -S:F8BT	Sol.	ITO S LiF Al	8.9	(blue)	n.a.
Seo 2010 [46]	C30 Alq <sub>3</sub>	Vac.	ITO S Al	10	410	>74
	C30:C <sub>60</sub>  Alq <sub>3</sub>			23	440	>82
	C30:C <sub>60</sub>  Alq <sub>3</sub>			64	440	>82
Antognazza 2010 [96]	MeLPPP:PCBM	Sol.	ITO S Al	1.1	470	61
Fukuda 2011 [92]	MDMO-PPV:F8BT	Sol.	ITO S LiF Al	2.4	(blue)	n.a.
Seo 2011 [47]	C30:C <sub>60</sub>	Vac.	ITO S NTCDA ITO	7.6	433	>90
Walker 2011 [74]	NK-3989 CdSe(NW)	Sol.	Pt Bi S Bi Pt (Planar)	n.a.	446	103
Yang 2011 [75]	PEDOT:PSS:NK-3989	Sol.	ITO S Al	≈10 <sup>-4</sup>	450	20
Fukuda 2012 [121]	NMe <sub>2</sub> -S:F8BT	Sol.	ITO S LiF Al	6.4	(blue)	n.a.
	EtCz-S:F8BT			8.4		
	NPh <sub>3</sub> -S:F8BT			52		
	NO <sub>2</sub> -S:F8BT			<1		
	PhCz-S:F8BT			<1		

Table 2. (Continued.)

Organic NBA photodetectors						
Article	Photoactive layer	Process	Architecture	$EQE_p$ %	$\lambda_p$ /(colour) nm/—	FWHM nm
Kimura 2012 [122]	EtCz-S:F8BT	Sol.	ITO S Al	27	(blue)	n.a.
Sakai 2012 [22]	NMe <sub>2</sub> -S:C30 Alq <sub>3</sub>	Vac.	ITO S Al	59	427	>90
Pandey 2014 [123]	D-5T-1:PCBM D-5T-2:PCBM	Sol.	ITO PEDOT:PSS S Al	22.5	435	>125
Sato 2014 [95]	F8T2:PCBM	Sol.	ITO FOPA S Al Ag	75	460	>150
Fedorov 2015 [77]	TC-PM	Sol.	C-CNTs S Ag	0.0025	465	n.a.
Sakai 2015 [111] Takagi 2016 [112]	C30:C <sub>60</sub>  Alq <sub>3</sub>	Vac.	IZO S ITO	n.a.	(blue)	n.a.
Li 2016 [71]	Rubrene:MoO <sub>3</sub> Rubrene C <sub>60</sub>	Vac.	ITO PEDOT:PSS S Al	55	(blue)	>133
Yoon 2016 [91]	ZnO F8T2	Sol.	ITO S MoO <sub>3</sub>  Au	4.5	467	114
Fedorov 2017 [78]	TC-PM	Sol.	Au S Au (planar)	n.a.	465	n.a.
Yoon 2018 [124]	ZnO PNa6-Th ZnO PNa6-Th:PCBM	Sol.	ITO S MoO <sub>3</sub>  Ag	5.4 37.8	412	>180 156
Sim 2018 [84]	F8T2 PCBM	Sol.	ITO MoO <sub>x</sub>  S Al	8.1	471	>108
Liess 2018 [79]	PEDOT:PSS M1(Pyrl) C <sub>60</sub> PEDOT:PSS M1(Pip) C <sub>60</sub>	Sol. and Vac.	ITO S Al	18 7	481 480	76 210
Aihara 2003 [44, 45]	R6G:PMPS	Sol.	ITO S Al	<0.8	506	111
Takada 2006 [52]	QA	n.a.	ITO EBL S ITO	n.a.	(green)	n.a.
Antognazza 2007 [97]	P3HT	Sol.	ITO S Al	≈0.1	564	116
Seo 2007 [54]†	DMQA Alq <sub>3</sub>	Vac.	ITO S NTCDA ITO	6	505	97
Lamprecht 2008 [68]	NPD DFPP	Vac.	Cr Au S Ag	2.2	545	89

Table 2. (Continued.)

Organic NBA photodetectors						
Article	Photoactive layer	Process	Architecture	$EQE_p$ %	$\lambda_p$ /(colour) nm/—	FWHM nm
Fukuda 2009 [49]	PFO:R6G	Sol.	ITO S LiF Al	$\approx 10^{-2}$	514	n.a.*
Aihara 2009 [55]	DMQA Py-PTC	Vac.	ITO S NTCDA ITO	5	510	132
Seo 2011 [47]	DMQA Py-PTC	Vac.	ITO S NTCDA ITO	7	501	133
Seo 2011 [56]†	DMQA Py-PTC	Vac.	ITO S NTCDA ITO	n.a.	532	94
Walker 2011 [74]	NK-2203 CdSe(NW)	Sol.	Pt Bi S Bi Pt (Planar)	n.a.	558	218
Yang 2011 [75]	PEDOT:PSS:NK-1952 PEDOT:PSS:NK-2203	Sol.	ITO S Al	n.a. n.a.	535 590	40 75
Fukuda 2012 [50]	PFO:R6G	Sol.	ITO PEDOT:PSS S Al	32.6	(green)	n.a.
Fukuda 2013 [51]	NMe2-S:R6G:PFO	Sol.	ITO GO S LiF Al	0.29	(green)	n.a.
Jansen-van Vuuren 2013 [125]	Kc:PCBM D-Kc-1:PCBM D-Kc-2:PCBM	Sol.	ITO PEDOT:PSS S Al	8 5.2 8.2	520 530 510	175 141 130
Lee 2013 [57]	DMQA:DCV3T	Vac.	ITO MoO <sub>x</sub>  S Al	67.6	540	153
Lee 2013 [58]	SubPc:F5SubPc SubPc:DCV3T DMQA:SubPc DMQA:F5SubPc	Vac.	ITO MoO <sub>x</sub>  S Al	49.2 62.6 60.1 52.2	550 540 560 580	137 211 131 126
Leem 2013 [59]	DMQA:DCV3T	Vac.	ITO TPD MoO <sub>x</sub>  S Al	55.2	540	146
Yang 2013 [76]	PEDOT:PSS:NK-2203 PCBM PEDOT:PSS:NK-1952 PCBM	Sol.	ITO PEDOT:PSS S Al	n.a. 0.4	595 540	8 >20
Kim 2014 [60]	DCV3T DCV3T:DMQA DMQA	Vac.	ITO Rb <sub>2</sub> CO <sub>3</sub>  S TAPC HATCN IZO	$\approx 5$	525	155*

Table 2. (Continued.)

Organic NBA photodetectors						
Article	Photoactive layer	Process	Architecture	$EQE_p$ %	$\lambda_p$ /(colour) nm/—	FWHM nm
Lee 2014 [61]	DMQA:DCV3T	Vac.	ITO MoO <sub>x</sub>  S Al	60.7	540	164
	DMQA:SubPc			60.1	540	129
Lim 2014 [27] ‡	TIPsAntTNa	Sol.	Au S Au (Planar)	>500 §	520	>140
Lim 2015 [11]	DM-DMQA:SubPc	Vac.	ITO MoO <sub>x</sub>  S Al	56.5	580	115
Sakai 2015 [111] † Takagi 2016 [112] †	spiro-2CBP QA	Vac.	IZO S Al	n.a.	(green)	n.a.
Bulliard 2016 [120]	NPIDDTh:C <sub>60</sub>	Vac.	ITO S MoO <sub>x</sub>  ITO	47.48	530	98
	NPBIDDTh:C <sub>60</sub>			51.98	550	101
Han 2016 [126]	M1:C <sub>60</sub>	Vac.	ITO HBL S ITO	42.4	520	89
	M2:C <sub>60</sub>		ITO HBL S ITO	44.3	520	106
	M3:C <sub>60</sub>		ITO HBL S ITO	38.8	530	96
	M4:C <sub>60</sub>		ITO HBL S ITO	48.6	550	99
	M4:C <sub>60</sub>		ITO EBL S ITO	48.6	550	97
Sung 2016 [127]	ZnO PP-TPD	Sol.	ITO S MoO <sub>3</sub>  Au	24	550	188
Sakai 2016 [53]	Alq <sub>3</sub>  QA Spiro-2CBP	Vac.	ITO S HAT-CN ITO Alq <sub>3</sub>	25	560	120*
				28.9		117
Heo 2017 [128]	NPIDDSe:C <sub>60</sub>	Vac.	ITO SiO <sub>x</sub> N <sub>y</sub>  S ITO	67	550	120
Satoh 2017 [129]	D:C <sub>60</sub>	Vac.	ITO S MoO <sub>x</sub>  ITO Al <sub>2</sub> O <sub>3</sub>  SiON  $\mu$ Ln	67	569	n.a.*
Sung 2017 [130]	ZnO PP-Th	Sol.	ITO S MoO <sub>3</sub>  Ag	13	510	100
Li 2017 [72]	PSQ	Vac.	ITO PEDOT:PSS S Al	66	600	110
Gao 2017 [131] ‡	ZMO-NPs BET	Sol.	Au Graphene S Graphene Au (Planar)	$1.9 \cdot 10^5$	530	50
Aihara 2003 [44, 45]	ZnPc Alq <sub>3</sub>	Vac.	ITO S Al	<20	616	174*

Table 2. (Continued.)

Organic NBA photodetectors						
Article	Photoactive layer	Process	Architecture	$EQE_p$ %	$\lambda_p$ /(colour) nm/—	FWHM nm
Antognazza 2007 [97]	VA	Sol.	ITO S Al	$\approx 0.1$	613	84*
Seo 2007 [54]†	ZnPc Alq <sub>3</sub>	Vac.	ITO S NTCDA ITO	5	597 ¶	>218
Fukuda 2009 [49]	PFO:Ni( <i>t</i> -Bu) <sub>4</sub> Pc	Sol.	ITO S LiF Al	$4.5 \cdot 10^{-4}$	607	70
Aihara 2009 [55]	ZnPc TiOPc BALq	Vac.	ITO S Al	20	646	253
Seo 2011 [47]	ZnPc TiOPc Alq <sub>3</sub>	Vac.	ITO S Al	18	731	>220*
Seo 2011 [56]†	ZnPc TiOPc Alq <sub>3</sub>	Vac.	ITO S ITO	n.a.	615	>110
Sakai 2013 [64]	spiro-2CBP ZnPc Alq <sub>3</sub>	Vac.	ITO S Al	n.a.	620	232*
Sakai 2015 [111]† Takagi 2016 [112]†	ZnPc	Vac.	IZO S LiF Al Au	n.a.	(red)	n.a.
Sakai 2016 [70]	SubNc spiro-2CBP SubNc Alq <sub>3</sub>	Vac.	IZO S Al	59 80	710 690	155 167*
Li 2016 [23]	ISQ ISQ C <sub>60</sub>	Vac.	ITO PEDOT:PSS S Al	15 7.8	680 680	80 179
Li 2016 [71]	ISQ	Vac.	ITO PEDOT:PSS S Al	55	680	87
Osedach 2012 [24]	U3 ZnO	Vac. and Sol.	ITO S MoO <sub>3</sub>  ITO Ag	16.1	756	133
Arca 2013 [73]	DaSQ:PCBM	Sol.	ITO PEDOT:PSS S Ca Ag	24.3	791	256*
Zhang 2015 [132]	poly-C <sub>60</sub>  C <sub>7</sub> -T	Vac.	ITO TiO <sub>2</sub>  S MeO-TPD MoO <sub>3</sub>  Au MoO <sub>3</sub>	13 23	850 850	133 141

**Table 3.** Organic input-filtered narrowband photodetectors from the literature. The entries are grouped into blue-, green- and red-responsive photodetectors, and are listed in chronological order within each of these groups. Process: sol. (solution-based); vac. (vacuum-based). S in the Architecture column denotes the photoactive layer.

Organic input-filtered photodetectors						
Article	Photoactive layer	Process	Architecture	$EQE_p$ %	$\lambda_p$ nm	FWHM nm
Yu 1998 [80]	P3OT:PCBM	Sol.	ITO S Al	$\approx 60$	430	64
Yu 2000 [81] Wang 2000 [82]	P3HT:PCBM	Sol.	ITO S Al	$\approx 23$	436	74
Ihama 2011 [133]	n.a.	Vac.	n.a.	$\approx 86$	440	>112
Yu 1998 [80]	P3OT:PCBM	Sol.	ITO S Al	$\approx 41$	528	63
Yu 2000 [81] Wang 2000 [82]	P3HT:PCBM	Sol.	ITO S Al	$\approx 20$	559	60
Ihama 2011 [133]	n.a.	Vac.	n.a.	$\approx 82$	530	138
Yu 1998 [80]	P3OT:PCBM	Sol.	ITO S Al	$\approx 44$	607	49
Yu 2000 [81] Wang 2000 [82]	P3HT:PCBM	Sol.	ITO S Al	$\approx 15$	611	39
Ihama 2011 [133]	n.a.	Vac.	n.a.	$\approx 80$	600	77
Deckman 2018 [83]	PV-D4650:PC <sub>70</sub> BM	Sol.	PEDOT:PSS PEIE S PEDOT:PSS	27 41	670 640	60 160

**Table 4.** Perovskite input-filtered narrowband photodetectors from the literature. † Filtering through stacking. S in the Architecture column denotes the photoactive layer. In the photoactive layer column, the following acronyms are used: SC (single crystal); PC (polycrystalline).

Perovskite input-filtered photodetectors						
Article	Photoactive layer	Process	Architecture	$EQE_p$ %	$\lambda_p$ nm	FWHM nm
Yakunin 2017 [113]†	MAPbBr <sub>3-x</sub> I <sub>x</sub> (SC)	SC growth (sol.)	Ag S Ag (Planar)	48.6	810	259
	MAPbBr <sub>3</sub> (SC)		Ag S Ag (Planar)	30.8	560	140
	MAPbCl <sub>3</sub> (SC)		Ag S Ag (Planar)	$6.3 \cdot 10^{-3}$	373	71
Li 2017 [134]	MAPbI <sub>3</sub> (PC)	Spin	ITO PTAA S PCBM C <sub>60</sub>  BCP Cu	18.6	766	33.7
	MAPbCl <sub>1.5</sub> Br <sub>1.5</sub> (PC)		n.a.	469	66	
	MAPbBr <sub>1.5</sub> I <sub>1.5</sub> (PC)		n.a.	594	105	
	MAPbI <sub>3</sub> (PC)		n.a.	614	77	

strategies (section 6.2); spectral ranges (section 6.3); photocurrent operational modes (section 6.4); and processing methods (section 6.5).

The analysis presented here is comprehensive insofar as it takes into account all the relevant literature—to the best of the author's knowledge. In keeping with the spirit of this review, the discussion concentrates on photodetectors that meet the minimum spectral rejection criterion, unless otherwise stated. Nonetheless, photodetectors that do not conform to this criterion but that are particularly responsive in a definite spectral region (e.g., colour-responsive photodetectors) are also referenced, as they provide a useful indication of the spectral limits of some materials and/or device configurations.

### 6.1. A materials perspective: organics versus perovskites

A comparison between the two semiconductor technologies covered in this review (i.e., organics and perovskites) is motivated by the need to pinpoint the strengths and weaknesses of each of them with regard to narrowband photodetection. This comparison, however, must confront the significant imbalance between the number of works pertaining to each of these two technologies (see tables 2–7). This imbalance partly reflects the later emergence of perovskites; while the bulk of narrowband organic photodetector research spans nearly two decades, the perovskite counterpart has taken place over only a handful of years. However, this imbalance also points to a key, inherent difference between the two semiconductor families. Indeed, perovskites feature broadband absorption and require

**Table 5.** Organic internally filtered narrowband photodetectors from the literature. The entries are grouped into blue-, green-, red- and NIR-responsive photodetectors, and are listed in chronological order within each of these groups. \*  $FWHM_{EQE}$  is ill-defined over the visible range, as  $SRR_{EQE} < 2$ . Process: sol. (solution-based); vac. (vacuum-based). S in the Architecture column denotes the photoactive layer.

Organic internally filtered photodetectors							
Article	Photoactive layer	Process	Config.	Architecture	$EQE_p$ %	$\lambda_p$ nm	FWHM nm
Iizuka 2000 [67]	CuPc BPPC	Vac.	IOEF PCL	Au S Al	2.56	489	88
	CuPc BPPC MC <sub>b</sub>			Au S Au	n.a.	489	83
Kudo 1981 [48]	ZnO MC <sub>a</sub>  RB	Vac.	IOEF PCL	ITO S Al	7	580	74*
Lyons 2014 [114]	Kc:PCBM C <sub>60</sub>	Vac. and Sol.	IOEF PCL	ITO MoO <sub>x</sub>  S LiF Al	17	536	90
	Kc2:PCBM C <sub>60</sub>				15	525	80
Zhong 2017 [86]	hPDI2:F8BT	Sol.	CCN	ITO ZnO S MoO <sub>x</sub>  Al	1.7	575	22
Sim 2018 [84]	F8T2 PCBM	Sol.	IOEF PCL	ITO MoO <sub>x</sub>  S Al	7.8	525	67
Lamprecht 2008 [68]	MPP CuPc	Vac.	IOEF PCL	Cr Au S Ag	2	630	112
Chen 2010 [115]	P3HT:PCBM	Sol.	CCN	PEDOT:PSS S Ca Al	27.4	660	91
Higashi 2010 [69]	P6T BP3T CuPc C <sub>60</sub>	Vac.	IOEF PCL	ITO S BCP Al	22	610	175
	P6T BP3T CuPc CuPc:C <sub>60</sub>  C <sub>60</sub>			ITO PEDOT:PSS S BCP Al	51	620	178
Antognazza 2010 [96]	P3HT	Sol.	IntF-1	ITO S Al	0.09	627	72
Arca 2013 [73]	P3HT:PCBM	Sol.	CCN	ITO PEDOT:PSS S Al	16–47	651–692	90–150
	P3HT PCPDTBT:PCBM		IOEF PCL	ITO S Ca Ag	28.6	660	211*
	P3HT		IntF-1	ITO S Al	13.6	640	36
Armin 2015 [98]	PCDTBT:PC <sub>70</sub> BM	Sol.	CCN	ITO PEDOT:PSS S C <sub>60</sub>  Al	18	670	80
Shen 2016 [33]	P3HT:PCBM:CdTe-QDs	Sol.	CCNx	ITO PVK S BCP Al	200	660	114
	P3HT:PCBM		CCN		9.8	670	85
Zhong 2017 [86]	hPDI3:F8BT	Sol.	CCN	ITO ZnO S MoO <sub>x</sub>  Al	1.5	600	19
	hPDI4:F8BT				0.7	615	16
	hPDI3-Pyr-hPDI3:F8BT				0.2	645	20
Miao 2017 [30]	P3HT:PCBM	Sol.	IntF-1x	ITO PFN-OX S Al	1640	665	23

Table 5. (Continued.)

Organic internally filtered photodetectors							
Article	Photoactive layer	Process	Config.	Architecture	$EQE_p$ %	$\lambda_p$ nm	FWHM nm
Wang 2017 [31]	P3HT:PC <sub>70</sub> BM	Sol.	IntF-1x	ITO PEDOT:PSS S Al	8180 53 500	650 650	29 28
Yoon 2018 [135]	ZnO PPDT2FBT	Sol.	IOEF PCL	ITO S MoO <sub>3</sub>  Ag	29	625	203*
Kim 2018 [85]	POPhDT2DFBT:PC <sub>70</sub> BM	Sol.	CCN	ITO ZnO S MoO <sub>3</sub>  Ag	3.6	650	80
Sim 2018 [84]	P3HT PCBM	Sol.	IOEF PCL	ITO MoO <sub>x</sub>  S Al	23.7	630	51
Wang 2018 [32]	P3HT:PC <sub>70</sub> BM	Sol.	IntF-1x	ITO PEDOT:PSS S Al	4100	620–700	≈30
Armin 2015 [98]	DPP-DTT:PC <sub>70</sub> BM	Sol.	CCN	ITO PEDOT:PSS S C <sub>60</sub>  Al	8	930	60
Shen 2016 [34]	PDTP-DFBT:PC <sub>70</sub> BM:PbS-QDs PDTP-DFBT:PC <sub>70</sub> BM	Sol.	CCNx CCN	ITO SnO <sub>2</sub>  PEIE S MoO <sub>3</sub>  Ag	183 15	890	≈50
Wang 2018 [32]	P3HT:PTB7-Th:PC <sub>70</sub> BM	Sol.	IntF-1x	ITO PEDOT:PSS S Al	2000	760–860	≈50
Miao 2018 [25]	P3HT:PTB7-Th:PCBM	Sol.	IntF-1x	ITO PFN-OX S Al	200	800	≈40

**Table 6.** Perovskite internally filtered narrowband photodetectors from the literature. The entries are listed in chronological order. S in the Architecture column denotes the photoactive layer. In the photoactive layer column, the following acronyms are used: SC (single crystal); PC (polycrystalline); CF (crystal film).

Perovskite internally filtered photodetectors							
Article	Photoactive layer	Process	Config.	Architecture	$EQE_p$ %	$\lambda_p$ nm	FWHM nm
Fang 2015 [116]	MAPbCl <sub>3</sub> (SC)	SC growth (sol.)	CCN	Ga S Au	0.2–1.6	428	11
	MAPbBr <sub>3-x</sub> Cl <sub>x</sub> (SC)					479	15
	MAPbBr <sub>3-x</sub> Cl <sub>x</sub> (SC)					536	15
	MAPbBr <sub>3</sub> (SC)					566	16
	MAPbI <sub>3-x</sub> Br <sub>x</sub> (SC)					592	19
	MAPbI <sub>3-x</sub> Br <sub>x</sub> (SC)					636	20
Lin 2015 [117]	MAPbBr <sub>1</sub> I <sub>2</sub> :RB	Spin	DA-CCN	ITO PEDOT:PSS S C <sub>60</sub>  LiF Ag	11.8	641	76
	MAPbBr <sub>2</sub> I <sub>1</sub> :PEIE					520	82
	MAPbBr <sub>1.6</sub> I <sub>1.4</sub> :PEIE					460	79
Saidaminov 2016 [28]	MAPbI <sub>3</sub>	PC film growth (sol.)	CCNx	ITO S ITO (Planar)	4 · 10 <sup>4</sup>	830	33
	MAPbBr <sub>3</sub>					n.a.	21
	MAPbBr <sub>2</sub> Cl <sub>1</sub>					n.a.	24
	MAPbCl <sub>3</sub>					n.a.	16
Rao 2017 [118]	MAPbBr <sub>3</sub> (CF)	Confined crystal film growth (sol.)	CCN	FTO S Au	18.5	567	30
Wu 2018 [119]	CsPbBr <sub>3</sub> (PC)	Centrif.	CCN	Au S Au (Planar)	13	546	14
	CsPbCl <sub>3-x</sub> Br <sub>x</sub> (PC)					n.a.	11
	CsPbCl <sub>3-x</sub> Br <sub>x</sub> (PC)					n.a.	13
	CsPbBr <sub>3-x</sub> I <sub>x</sub> (PC)					n.a.	27.3
	CsPbBr <sub>3-x</sub> I <sub>x</sub> (PC)					n.a.	31
	CsPbBr <sub>3-x</sub> I <sub>x</sub> (PC)					n.a.	39

**Table 7.** Organic microcavity-based narrowband photodetectors from the literature. The entries are grouped into blue-, green-, red- and NIR-responsive photodetectors, and are listed in chronological order within each of these groups. † With input filtering. § The spectral response below 435 nm was not reported. # Input filtering needed to achieve narrowband response over the whole visible and NIR range. Process: sol. (solution-based); vac. (vacuum-based). S in the Architecture column denotes the photoactive layer.

Organic microcavity-based photodetectors						
Article	Photoactive layer	Process	Architecture	$EQE_p$ %	$\lambda_p$ /(colour) nm/—	FWHM nm
Lupton 2003 [136]	MeLPPP C <sub>60</sub>	Vac. and Sol.	DBR ITO S Ag	n.a.	495	16 §
An 2009 [137]	NPD C <sub>60</sub>	Vac.	Al MoO <sub>3</sub>  S BCP Ag	9.1	452	46
Koepppe 2003 [138]	MeLPPP C <sub>60</sub>	Vac. and Sol.	Ag S Al Ag	0.03–0.05	535–575	≈35 #
Lupton 2003 [136]	MeLPPP C <sub>60</sub>	Vac. and Sol.	Ag S Ag	0.03–0.12	530–600	≈35–70 #
An 2009 [137]	CuPc C <sub>60</sub>	Vac.	Al MoO <sub>3</sub>  S BCP Ag	11.8	520	51 #
Tang 2017 [42]	PBTTT:PCBM	Sol.	Au PEIE S MoO <sub>3</sub>  Ag	30–50	630–710	20–40 #
	PBTTT:PCBM		PEDOT:PSS PEIE S MoO <sub>3</sub>  Ag	43	715	19 #
	P3HT:PCBM		Au PEIE S MoO <sub>3</sub>  Ag	9.3	710	≈50 #
	PBTTT:PCBM		Au PEIE S MoO <sub>3</sub>  Ag	n.a.	705–740	30–55 #
Siegmund 2017 [65]†	ZnPc:C <sub>60</sub>	Vac.	Ag ETL S HTL MoO <sub>3</sub>  Au Ag F <sup>a</sup>	1.4–22.5	870–1085	35–43
Siegmund 2017 [65]	TPDP:C <sub>60</sub>	Vac.	Ag ETL S HTL MoO <sub>3</sub>  Au Ag MoO <sub>3</sub>  Alq <sub>3</sub> <sup>b</sup>	3–20	810–1550	40–70 #
Tang 2017 [42]	PBTTT:PCBM	Sol.	Au PEIE S MoO <sub>3</sub>  Ag	10–32	750–975	20–40 #
	PBTTT:PCBM		PEDOT:PSS PEIE S MoO <sub>3</sub>  Ag	25–41	770–907	14–15 #
	P3HT:PCBM		Au PEIE S MoO <sub>3</sub>  Ag	0.2–4.3	750–970	≈50 #
	PDPPTDTPPT:SdiCNPBI		Au PEIE S MoO <sub>3</sub>  Ag	10 <sup>-2</sup> –2	1000–1680	30–45 #
	PBTTT:PCBM		Au PEIE S MoO <sub>3</sub>  Ag	n.a.	790–1065	≈50 #
Ullbrich 2017 [139]	ZnPc:C <sub>60</sub>	Vac.	Ag ETL S HTL MoO <sub>3</sub>  Au Ag MoO <sub>3</sub>  Alq <sub>3</sub> <sup>c</sup>	4	1055	≈45 #
	ZnPc ZnPc:C <sub>60</sub>  C <sub>60</sub>		0.3	1065		

<sup>a</sup> ETL: Bis-HFI-NTCDI:W<sub>2</sub>(hpp)<sub>4</sub>C<sub>60</sub>; HTL: ZnPc|BF-DPB:NDP9; F: C<sub>60</sub>|ZnPc.

<sup>b</sup> ETL: BPhen:C<sub>60</sub>; HTL:p-BF-DPB.

<sup>c</sup> ETL: BPhen:C<sub>60</sub>; HTL: BF-DPB:NDP9.

filtered strategies for narrowband photodetection to be achieved. In many ways, such strategies link—either directly or indirectly—to challenges associated with conventional semiconductor technologies (see section 1). Therefore, the inherent broadband absorption character of perovskite semiconductors has curbed the interest in their application to narrowband photodetection (as also revealed by the much larger number of publications on broadband perovskite photodetectors). On the other hand, organic semiconductors boast a large body of narrowband absorbers. Such a conspicuous subset of organic semiconductors enables NBA-type photodetection, which can potentially overcome the challenges and limitations of conventional filtered strategies (section 5.1). Indeed, the primary driving force of narrowband organic photodetection research arises precisely from this aspect, as confirmed by the predominance of NBA-type works across the organic narrowband literature (see tables 2, 3, 5, 7).

Notwithstanding their broadband absorption character, perovskites have been successfully harnessed (through filtered strategies) in narrowband photodetectors, thanks to their spectral tunability via facile compositional tailoring (see tables 4, 6). Indeed, a central aspect of most perovskite works is the ability to tailor the photodetector passbands through the visible and the NIR range by simply replacing the halide in the photoactive material, while keeping the same procedures for material preparation, deposition, and device fabrication [28, 113, 116, 117, 119, 134]. For example, in several works,  $\text{APbCl}_3$  and  $\text{APbBr}_{3-x}\text{Cl}_x$  ( $A = \text{MA}$  or  $\text{Cs}$ ) have been used for blue-selective photodetectors due to their absorption onset in this region [28, 116, 119]. Along similar lines,  $\text{APbBr}_3$  has been used for green-selective photodetectors [28, 116, 118, 119],  $\text{APbBr}_{3-x}\text{I}_x$  for red-selective photodetectors [116, 119], and  $\text{APbI}_3$  for NIR-selective photodetectors [28] ( $A = \text{MA}$  or  $\text{Cs}$ ).

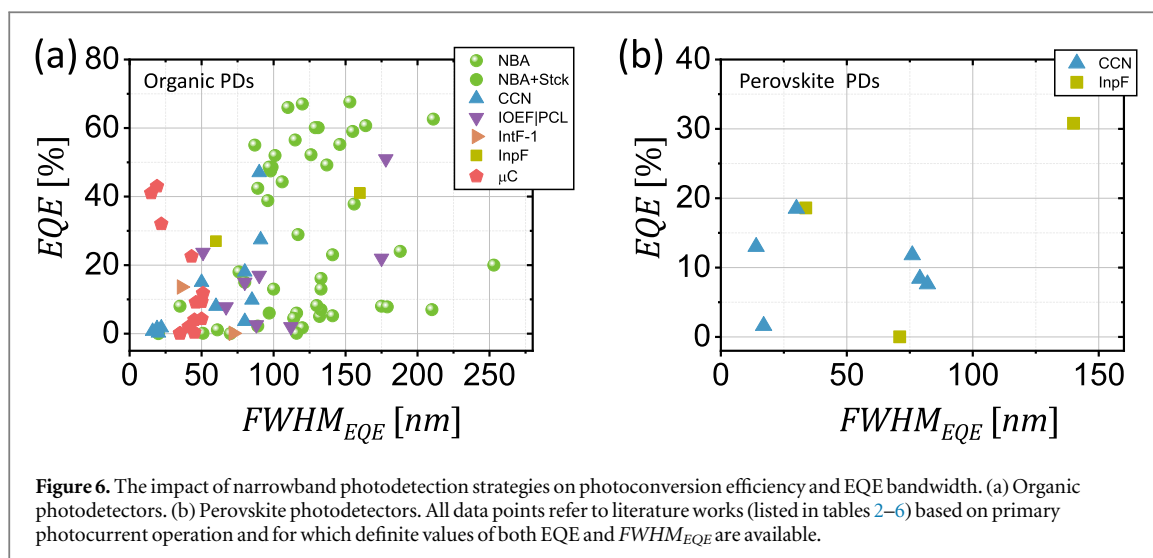
In terms of device performance, perovskite-based narrowband photodetectors have achieved ultranarrowband response ( $\text{FWHM}_{\text{EQE}} < 50\text{nm}$ ) in a number of works through the visible and the NIR range [28, 116, 118, 119, 134], and in some cases EQE widths as low as 11–16 nm have been reported [28, 116, 119]. The lowest values reflect the characteristic sharp absorption onsets of the corresponding perovskites. Rather wide EQE widths (150–250 nm) [113] have also been attained in other device configurations.

From a photoconversion efficiency point of view, ultranarrowband perovskite photodetectors have typically provided modest EQE figures, i.e., in the 5%–18% range [116, 118, 119]. Higher EQE figures (up to 48%) in primary photocurrent mode have only been achieved in one instance [113]. As expected, secondary photocurrent operation has enabled significantly greater figures (up to  $4 \cdot 10^4\%$  in one instance) [28, 113]. Of course, the latter are the direct consequence of a mechanism enabled by carrier injection from the contacts (as opposed to an inherently efficient photoconversion process) (section 3.1).

Organic narrowband photodetector works offer a significantly more varied landscape than their perovskite counterparts. This primarily arises from the available diversity of materials and the corresponding absorption properties, which also enable a wider range of narrowband strategies (see section 4 and tables 2, 3, 5, 7). EQE values (in primary photocurrent mode) in the 50%–80% range have been achieved throughout the visible range [11, 22, 46, 57–59, 61, 69–72, 95, 120, 121, 128, 129], with associated spectral widths of around 90–150 nm. Operation in secondary photocurrent mode has also delivered large EQE values [27, 30–32, 131], typically in the  $10^3\%$ – $10^4\%$  range, and up to  $\approx 2 \cdot 10^5$  in one instance [131]. Ultranarrowband photodetectors ( $\text{FWHM}_{\text{EQE}} < 50\text{nm}$ ) have also been obtained in a conspicuous number of works [25, 30–32, 42, 54, 65, 73, 75, 76, 80–82, 86, 136–139].

A characteristic aspect of the majority of organic works is their use of the NBA approach, as justified by its attractiveness for narrowband photodetection (section 5.1). Considering that perovskite semiconductors are precluded from the NBA approach, a straightforward performance comparison between organic and perovskite narrowband photodetectors is not viable. Indeed, as discussed subsequently (section 6.2), narrowband photodetector performance is closely related to the adopted narrowband strategies. Consequently, a strategy-specific discussion (section 6.2) is needed for the comparison to become meaningful. For the time being, we note that the CCN approach (which is dominant in perovskite works) has generally delivered photoconversion efficiencies (in primary photocurrent mode) lower than the NBA strategy, regardless of the semiconductor employed. Therefore, the capability of organic semiconductors to rely on NBA-type strategy (due to the narrowband absorption character of many of them) gives them an advantage for applications that require particularly high photoconversion efficiencies in primary photocurrent mode. From the point of view of EQE width instead both semiconductor families are able to deliver the same width ranges, as evidenced by the figures reported earlier.

A final aspect of particular importance when comparing organic and perovskite narrowband photodetectors concerns the thickness of the photoactive layers required by these two semiconductor technologies. While not a direct determinant of the performance figures considered in our discussion, the photoactive layer thickness plays an important role in defining the performance scope of organic/perovskites photodetectors for relevant applications (*vide infra*). The majority of perovskite works rely on particularly thick photoactive layers (e.g., hundreds to thousands of micrometres). This arises either from the use of monocrystalline layers, or from the adoption of basic CCN strategy. In the latter case, the requirement of having a particularly thick photoactive layer originates from the long photocarrier drift length characteristic of perovskites. Thinner (sub-micrometre) perovskite device stacks have been demonstrated in only one work (DA-CCN-type) [117], and rely on the blending of a perovskite with an organic material so as to reduce the photocarrier drift length. In contrast, organic narrowband photodetectors most often



comprise photoactive layers with a thickness of a few hundred nanometres (due to their optoelectronic properties and/or the broader range of viable narrowband strategies). Thin (i.e., submicrometre) photoactive layers are particularly needed to realise high-performance imagers capable of overcoming the resolution limitations of conventional (e.g., silicon-based) technologies [133, 140]. Additionally, thick mono/poly-crystalline perovskite layers are expected to inhibit the realisation of flexible photodetectors (due to mechanical failure), which are sought after for a number of emerging applications. In contrast, the mechanical flexibility of organic narrowband photodetectors has been demonstrated in a few studies [23, 83, 131]. Therefore, at the state of the art, organic narrowband photodetectors possess an important edge in terms of potential to deliver attractive performance figures for high-resolution imaging and/or applications requiring mechanical flexibility.

## 6.2. Impact of narrowband strategies

The particular narrowband strategies adopted are a key determinant of the performance of a narrowband photodetector technology. Here we discuss the relevant trends, highlighting the solutions that have been especially successful.

In the context of organic semiconductors, the NBA strategy is predominant in the visible range. The reasons for this are manifold: (a) the ease and attractiveness of the NBA approach to achieve narrowband photodetection (section 5.1); (b) the later development of CCN and microcavity approaches; (c) the limited edge of the input-filtered strategy (in view of its overlap with conventional narrowband photodetection, with which it shares similar challenges). In primary photocurrent mode, the NBA strategy has led to the highest EQE figures of all narrowband approaches (up to 60%–80%), as exemplified by figure 6(a) [46, 57, 58, 61, 70, 95, 128, 129]. This can be rationalised in terms of its straightforward operation, which does not require filtering and/or the introduction of deliberate loss mechanisms. Indeed, in an NBA-type device all photons within the target spectral region are allowed into the photoactive material through a transparent input electrode, and recombination losses are kept to a minimum due to having a photoactive layer thickness comparable with the in-band absorption depth.

As exemplified by figure 6(a), internally filtered and microcavity-based organic photodetectors generally feature lower EQE figures than their NBA counterparts (again, we refer to primary photocurrent operation due to its direct relationship to the intrinsic photoconversion capabilities of the photoactive material). Within the realm of internally filtered devices, the highest EQE of IntF-1 devices is at 13.6% [73]; IOEF|PCL generally perform below 30% [48, 67, 68, 73, 84, 114, 135] (with the exception of the work of Higashi *et al* which reaches 51% with an optimised architecture) [69]; CCN works typically give EQEs in the 1%–20% range [33, 34, 85, 86, 98] (the work of Arca *et al* reaching an EQE of 47%, is an important exception) [73]. The EQEs of most microcavity-based photodetectors are less or much less than 25% [42, 65, 136–139] (the only exception being found in the work of Tang *et al* [42] who achieved EQEs up to 50% through detailed modelling and design). This is reflective of the fact that internally filtered and microcavity-based strategies are typically prone to greater photoconversion losses. For instance, the transmittance of the IOEF layer of internally filtered photodetectors may be  $<100\%$  within the target spectral range. In addition, internally filtered devices may incur comparatively greater recombination losses due to the longer path (through the IOEF) that photocarriers need to travel (e.g., consider the thick layers required in IntF-1 and CCN devices). Finally, microcavity devices are affected by losses due to the use of a reflective input electrode, which limits the amount of light entering the photoactive volume; the finite absorbance of their electrodes, which limits the enhancement of the

resonant optical field; and the need of an input filter to achieve truly narrowband photodetection over the full spectral reference range, which may introduce further losses due to a transmittance  $< 100\%$  within the target spectral range.

A full assessment of the photoconversion efficiency of input-filtered organic photodetectors is generally not possible, as works that have pursued this strategy typically provide only the EQE of the underlying broadband photodetector [80–82, 133]. The only confirmed figures—in the 20%–40% range—are from the work of Deckman *et al* [83]. Drawing from conventional (e.g., silicon-based) input-filtered technologies, a transmittance  $< 100\%$  of the filter materials within the target spectral range (a key loss mechanism of this approach) is likely to pose an important limitation on the EQE of the resulting photodetectors.

Photoconversion efficiency data from perovskite devices is consistent with the picture emerging from organic photodetector works (figure 6(b)). Perovskite-based CCN devices have EQEs generally not higher than  $\approx 20\%$  [116–119], just as for their organic counterparts (the sole exception is found in the devices of Saidaminov *et al* [28], which, however, do not operate in primary photocurrent mode). The EQE figures from input-filtered devices are at 20%–50% (also similar to their organic counterpart). The consistency between the figures from CCN and input-filtered devices made with organic and perovskite semiconductors suggests that the adopted narrowband strategies are key determinants of the resulting photoconversion efficiency. Additionally, it points to the fact that filtered approaches generally pose a limit on the achievable photoconversion efficiency—the highest EQE figures of all organic and perovskite narrowband photodetectors are indeed obtained with organic NBA-type devices.

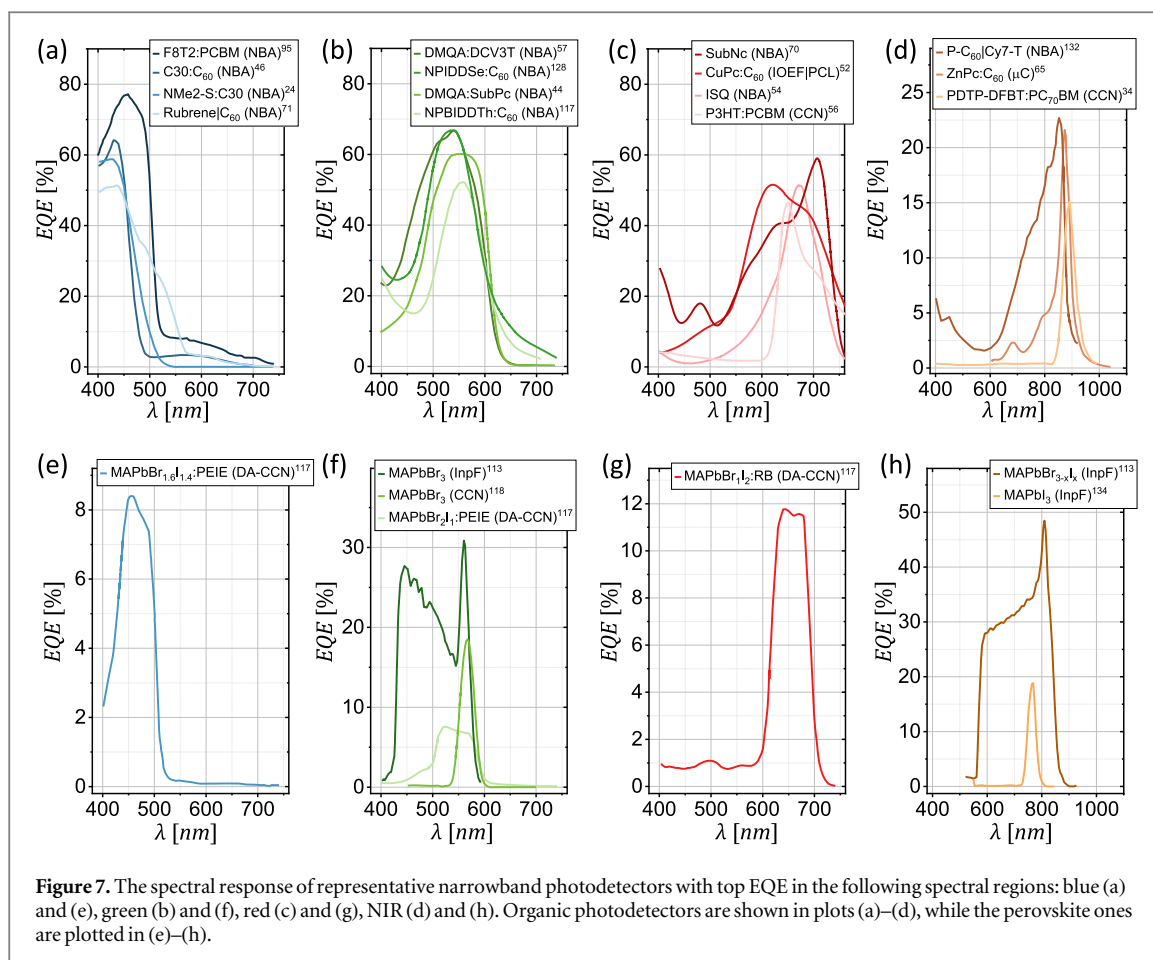
In terms of spectral bandwidth, significant progress at the material level has allowed (organic) NBA devices to reach  $FWHM_{EQE}$  values of about 100 nm and below (cf.  $FWHM_{EQE}$  of 130–200 nm of many earlier NBA-type works, as listed in table 2). This is exemplified in figure 6(a). These values are fully compatible with applications such as colour imaging for consumer electronic devices, as well as more demanding applications, e.g., computer vision. Particularly successful implementations have relied on dedicated molecular design strategies, e.g., D-A molecules approaching the cyanine limit ( $FWHM_{EQE} \approx 90\text{--}100$  nm) [120, 126]. Additionally, two important schemes relating to aggregation effects in the solid state have emerged as highly effective for achieving NBA-type photodetection with EQE widths well below 100 nm. One such scheme involves the use of J-aggregating and H-aggregating small molecules. This has been demonstrated to lead to  $FWHM \approx 10\text{--}75$  nm [75, 76, 79]. Alternatively, ultranarrowband NBA-type photodetection can be attained by preventing aggregation effects altogether [131]. This concept was implemented through a photoactive layer in which organic molecules are placed sufficiently apart from each other while anchored onto metal-oxide nanoparticles (cf., tightly packed small molecules in a film). A  $FWHM_{EQE}$  of 50 nm was achieved in such a case [131].

While requiring particular arrangements with organic NBA-type devices,  $FWHM_{EQE}$  figures (well) below 100 nm are the norm when employing the CCN approach, regardless of whether the photoactive material is organic or perovskite (figure 6) [28, 33, 34, 73, 85, 86, 98, 115–119]. The smallest EQE width across organic works was achieved by Zhong *et al* ( $FWHM_{EQE} \approx 15\text{--}20$  nm) with organic blends featuring particularly sharp absorption onsets [86]. Ultranarrowband behaviour is significantly more common with perovskite-based CCN devices, which typically feature  $FWHM_{EQE} \approx 10\text{--}20$  nm, likely due to their generally sharper onsets than the average organic counterpart [28, 116, 119]. An additional feature of CCN devices is their particularly high rejection ratio (arising from their robust filtering of photons outside the target spectral range), which, in fact, is desirable for many applications.

Other internally filtered strategies provide a varied bandwidth performance, as determined by the particular configuration employed. Nearly all IntF-1 organic works are at the ultranarrowband level ( $FWHM_{EQE} \approx 20\text{--}50$  nm), while achieving high rejection just as for CCN devices [25, 30–32, 73]. IOEF|PCL devices instead span a significantly wider  $FWHM_{EQE}$  range ( $\approx 50\text{--}180$  nm, see figure 6(a)) [67–69, 84, 114], as determined by the particular selection of optoelectronic filter materials.

Just as for IOEF|PCL devices, input-filtered (both organic and perovskite) devices exhibit varied spectral performance in view of their dependence on the spectral properties of the input filter. Organic implementations feature bandwidths well below 100 nm in a few cases [80–83], just as some of their perovskite counterparts [113, 134]. Some others instead are significantly larger ( $\approx 100\text{--}200$  nm), also regardless of the photoactive material employed (i.e., organic or perovskite) [83, 113, 133, 134].

Microcavity-based (organic) photodetectors fare well in terms of spectral width, with most implementations delivering ultranarrowband behaviour ( $FWHM_{EQE} \approx 15\text{--}50$  nm, see figure 6(a)) [42, 65, 136–139]. It is important to note, however, that microcavity-based devices also provide significant photoresponse in the spectral range where the photoactive material absorbs appreciably. Therefore, many of the quoted EQE width values in figure 6(a) only truly hold (with good spectral rejection achieved) if such devices are equipped with suitable input filtering to suppress their off-resonance response.



### 6.3. Spectral ranges

In this section the EQE and bandwidth of organic and perovskite narrowband photodetectors are discussed in reference to the following spectral regions: 400–500 nm (blue), 500–600 nm (green), 600–740 nm (red) and 740–2000 nm (NIR). This allows us to identify the most promising solutions specific to each of these spectral regions, which are particularly significant for manifold applications (section 1).

#### 6.3.1. Blue-selective photodetectors (400–500 nm)

The highest EQE values of organic narrowband photodetectors in the blue have been obtained via NBA-type devices. Polyfluorenes such as F8BT and F8T2 are employed in some of the highest performance works ( $EQE_p = 75\%$  with F8T2:PCBM [95], see figure 7(a), and  $EQE_p = 52\%$  with NPH<sub>3</sub>-S:F8BT [121]). Other high performance solutions include coumarin-based photoactive layers (64% with C30:C<sub>60</sub> [46], and 59% with NMe<sub>2</sub>-S:C30 [22], see figure 7(a)). Finally, a particularly high EQE (55%) was also obtained with a Rubrene:MoO<sub>3</sub>|Rubrene|C<sub>60</sub> device stack (figure 7(a)) [71]. Other organic works (regardless of the particular narrowband configuration adopted) generally deliver smaller EQEs, most typically below 10% [44, 45, 47–49, 54, 67, 75, 77, 84, 91–94, 96, 97, 137].

The highest efficiency of blue-selective perovskite photodetectors (8.4%) was reported by Lin *et al* and relied on the blending of MAPbBr<sub>1.6</sub>I<sub>1.4</sub> with PEIE to realise a DA-CCN device (figure 7(e)) [117]. Other reported EQE figures of blue-selective perovskite photodetectors (single crystals of MAPbCl<sub>3</sub> or MAPbBr<sub>3-x</sub>Cl<sub>x</sub>) are below 1% [113, 116].

The spectral width of blue-selective organic photodetectors is typically below  $FWHM_{EQE} < 100$  nm regardless of the narrowband strategy employed [54, 67, 75, 79–82, 96, 97, 136, 137]. In addition, ultranarrowband performance ( $FWHM_{EQE} < 50$  nm) was achieved via microcavity-based devices featuring MeLPPP|C<sub>60</sub> ( $FWHM_{EQE} = 16$  nm) and NPD|C<sub>60</sub> photoactive layers ( $FWHM_{EQE} = 46$  nm) [136, 137]. A particularly significant ultranarrowband work is that of Yang *et al* who achieved the lowest FWHM (20 nm) with the NBA approach thanks to the use of a J-aggregating cyanine dye [75].

Blue-selective perovskite devices generally deliver particularly narrow spectral responses, thanks to the widespread adoption of the CCN approach. The single-crystal photoactive layers of Fan *et al* give a FWHM of

11–15 nm [116]; the polycrystalline devices of Saidaminov *et al* and Wu *et al* are at 11–24 nm [28, 119]. Wider passbands are also possible, for instance, via DA-CCN (79 nm) [117], or via input filtering (70 nm) [134].

### 6.3.2. Green-selective photodetectors (500–600 nm)

Organic green-selective photodetectors have achieved the highest quantum efficiency (>50%) in primary-photocurrent mode through the NBA approach [11, 57–59, 61, 120, 128, 129, 133]. A large number of these works rely on green-absorbing quinacridone dye derivatives (used as donors) [11, 57–59, 61], leading to a maximum  $EQE_p$  of 67.6% in combination with green-absorbing DCV3T (used as an acceptor) (figure 7(b)) [57]. Chloroboron subphthalocyanine (SubPc) is another small molecule that has delivered high phototransduction efficiency in a number of works, giving an  $EQE_p$  of 62.6% in combination with DCV3T [58], and 60.1% in combination with quinacridone [58, 61] (figure 7(b)). Newly synthesised small-molecule donors featuring a D-A structure approaching the cyanine limit have also yielded EQE values in the  $\approx$ 50%–70% range in combination with fullerenes (figure 7(b)) [120, 126, 128, 129]. Finally, Li *et al* demonstrated the potential of a single-component squaraine photoactive layer, achieving an  $EQE_p$  as high as 66% [72]. Devices operating in secondary photocurrent mode have also been particularly successful, such as the ones of Gao *et al*, which reached an EQE up to  $1.9 \cdot 10^5\%$  with BET molecules anchored onto  $Zn_{0.9}Mg_{0.1}O$  nanoparticles [131].

Perovskite photodetectors that selectively respond to green light have predominantly relied on  $APbBr_{3-x}Cl_x$  [116],  $APbBr_3$  [28, 113, 116, 118, 119], and  $APbI_{3-x}Br_x$  [116, 119, 134], (A: Cs or MA) in view of the absorption onset in the green of these materials. Additionally, Lin *et al* also demonstrated that the use of  $MAPbBr_2I$  blended with PEIE achieves green-selective dual-absorption CCN photodetection. Of all reported implementations the highest EQE is at 30.8%, and was obtained from input-filtered perovskite-only single-crystal devices (figure 7(f)) [113].

The spectral width of green-selective organic photodetectors spans an especially wide range, due to the manifold narrowband approaches and material systems adopted. A considerable number of NBA-type devices feature a  $FWHM_{EQE}$  greater than 100 nm. A recurrent feature of many of them is the use of fullerenes, which generally broaden the spectral width and/or reduce the spectral rejection ratio (e.g., with respect to the blue, see figure 7(b)) [120, 125, 126, 128, 129]. A number of fullerene-free strategies have thus been considered to overcome this challenge and achieve  $FWHM_{EQE}$  values around or below 100 nm. One such strategy involves the use of donor-acceptor photoactive layers in which either of the component materials is transparent [68, 127, 130]. A representative example of this approach is in the work of Sung *et al*, where a green-absorbing polymer (serving as a donor) is combined with transparent ZnO (serving as an acceptor) to achieve a  $FWHM_{EQE}$  of  $\approx$ 100 nm [130]. Going one step further in this direction, Gao *et al* demonstrated a  $FWHM_{EQE}$  of 50 nm utilising a green-absorbing molecule (as a donor) in combination with transparent ZMO nanoparticles (as an acceptor), and preventing aggregation-induced broadening of the molecular absorber [131]. Narrow passbands (down to 115 nm [11]) and relatively high rejection ratios have also been enabled by donor-acceptor photoactive layers in which both components absorb in the green [11, 57–61]. A further successful (fullerene-free) strategy is found in the work of Li *et al* where a single-component green-absorbing photoactive layer was adopted to achieve a  $FWHM_{EQE}$  of 110 nm [72].

Looking beyond NBA-type organic devices, green-selective organic photodetectors have achieved significantly narrow passbands (60–75 nm) via input filtering [80–82]. Internal filtering has been equally successful, with widths in the 60–80 nm range via IOEF|PCL [48, 84, 114], and down to 22 nm through CCN [86]. Green-selective microcavity-based devices have been demonstrated as capable of ultranarrowband photodetection ( $FWHM_{EQE}$  at 35–50 nm) [136–138], provided that they are combined with input filtering to suppress their off-resonance response.

The EQE widths of green-selective perovskite photodetectors are in the same region as their blue-selective counterparts, resulting from the same narrowband strategies (input-filtering and CCN) being adopted in both wavelength ranges. Widths obtained from basic CCN devices are in the 14–30 nm region [28, 116, 118, 119], consequently being suitable for multispectral/hyperspectral applications. The DA-CCN devices of Lin *et al* instead achieve an 82 nm width, specifically intended to address colour detection applications [117]. Input-filtered devices generally provide wider passbands, as determined by the combined spectral properties of the photoactive and filter materials—e.g., Yakunin *et al* and Li *et al* reported widths of 140 nm and 105 nm by using a blue-selective photodetector [113] and a suitable perovskite layer [134] as input filters, respectively.

### 6.3.3. Red-selective photodetectors (600–740 nm)

NBA-type red-selective organic photodetectors have achieved particularly high EQEs. For instance, Sakai *et al* reported an EQE as high as 59% with a single-component photoactive layer made with red-absorbing chloroboron sub-2,3-naphthalocyanine (SubNc) (figure 7(c)) [70]. Also using the NBA strategy, Li *et al* achieved a peak EQE of 55% through a single-component squaraine layer (figure 7(c)) [71]. Other works that have also delivered high EQE in the red involve internal filtering. A representative case is from the work of Higashi *et al* relying on a  $CuPc:C_{60}$

BHJ as the photoconversion layer within an IOEF|PCL configuration, leading to an EQE of 51% (figure 7(c)) [69]. Additional examples of particularly efficient internally filtered photodetectors are CCN-type P3HT:PCBM devices operating in primary photocurrent ( $EQE_p = 47\%$ ) (figure 7(b)) [73], and IntF-1-type P3HT:PC<sub>70</sub>BM devices operating in secondary photocurrent mode ( $EQE_p = 53\,500\%$ ) [31]. Finally, efficient microcavity-based red-responsive devices have been realised by harvesting CT excitons within a PBTTT:PCBM photoactive layer ( $EQE_p = 50\%$ ) [42].

Perovskite-based devices selective to the red have been explored with photoactive layers made of APbI<sub>3-x</sub>Br<sub>x</sub> (A = MA/Cs) [116, 119], MAPbI<sub>3</sub> [134], and a blend of MAPbBr<sub>3</sub>I<sub>2</sub> and rhodamine B [117]. The highest confirmed EQE (11.8%) was obtained with the latter photoactive layer, which was utilised within a DA-CCN device (figure 7(g)).

The spectral width of organic red-responsive photodetectors varies greatly depending on the narrowband approach adopted. Among high-efficiency NBA photodetectors, the narrowest spectral bandwidth ( $FWHM_{EQE} = 87$  nm) is from the work of Li *et al* which employs a single-component squaraine layer (figure 7(c)) [71]. The spectral width of other NBA photodetectors is most typically greater/much greater than 100 nm [55, 70], and the minimum spectral rejection criterion is not met in many instances [44, 45, 47, 64, 70, 97]. This is indicative of the greater challenge of achieving narrowband photodetection in the red with NBA-type organic photodetectors, e.g., compared to their counterparts in the green and blue. Filtered devices perform to narrower spectral passbands, as guaranteed by inherent dissipation of their out-of-passband photons. The spectral width of input-filtered devices made with various photoactive layers is typically at 40–80 nm [80–83, 133]; single-component internally filtered devices with gain based on P3HT:PCBM and P3HT:PC<sub>70</sub>BM give widths of 20–30 nm [30–32]; CCN devices are typically below 90 nm [33, 73, 85, 98, 115], and reach down to about 15–20 nm in the work of Zhong *et al* (F8BT blended with PDI nanoribbons) [86]. Finally, microcavity-based devices based on PBTTT:PCBM attain widths down to about 20 nm, provided that input filtering is concomitantly used [42].

The spectral width of red-selective perovskite photodetectors is narrowest (20 nm) in the single-crystal CCN devices of Fang *et al* [116]. Other implementations give larger values (30–80 nm) [117, 119, 134], either by design (see the DA-CCN devices of Lin *et al* [117] and the input-filtered devices of Li *et al* [134]), or due to the specifics of the absorption edge (see CCN devices based on polycrystalline films of Wu *et al* [119]).

#### 6.3.4. NIR-selective photodetectors (740–2000 nm)

Narrowband NIR photodetection via organic semiconductors has been pursued in a comparatively limited number of works. The devices providing the highest peak EQE (41% in primary photocurrent mode) are the ones reported by Tang *et al* [42], which rely on the CT state absorption of PBTTT:PCBM in the microcavity configuration and use a distributed Bragg reflector (DBR) to boost performance. NBA devices deliver good but lower photoconversion efficiency [24, 73, 132], the highest (23%) being achieved with a cyanine dye in a planar heterojunction with polymerized C<sub>60</sub> (figure 7(d)). Note that the slightly higher EQE, 24.3%, achieved with DaSQ in [73] does not meet the minimum spectral rejection criterion over the visible–NIR reference range. The limited number of NBA works in the NIR range compared to the significantly larger number in the visible range reflects the smaller number of suitable compounds available to date with narrowband absorption in this region. While NIR-selective CCN devices operating in primary photocurrent mode have delivered generally lower performance (the highest EQE being at 15% with a PDTP-DFBT:PC<sub>70</sub>BM active layer, figure 7(d)) [34], operation in secondary photocurrent mode has led to EQE values up to 2000% through blends of P3HT:PTB7-Th:PC<sub>70</sub>BM [32].

Perovskite photodetectors with narrowband responsivity in the NIR range have been realised with photoactive layers made of MAPbI<sub>3</sub> [28, 134] and MAPbBr<sub>3-x</sub>I<sub>x</sub> [113]. The highest reported efficiencies ( $\approx 20\%$ – $50\%$ ) in primary photocurrent mode have been obtained with an input-filtered device (figure 7(h)) [113, 134]. CCN devices with gain instead have enabled EQE values as high as  $4 \cdot 10^4\%$  [28].

In terms of EQE width, NIR-selective organic photodetectors relying on the NBA strategy have delivered 130–140 nm at best [24, 132]. The CCN counterpart instead has afforded ultranarrowband response in the 40–60 nm range [25, 32, 34, 98]. The narrowest passbands of all organic devices have been attained with microcavity-based devices harvesting CT photons at resonance. This result was achieved by Tang *et al*, who demonstrated NIR-selective PBTTT:PCBM devices with widths of 20–40 nm using reflective electrodes, and down to 14–15 nm using a DBR [42]. As noted earlier, microcavity-based devices necessitate input filtering to achieve true narrowband operation across the whole visible–NIR range.

NIR-selective perovskite photodetectors have been demonstrated with widths of about 30 nm (both via input filtering [134] and CCN [28]). A significantly larger width (259 nm) was reported in a work based on stacked input-filtered devices [113].

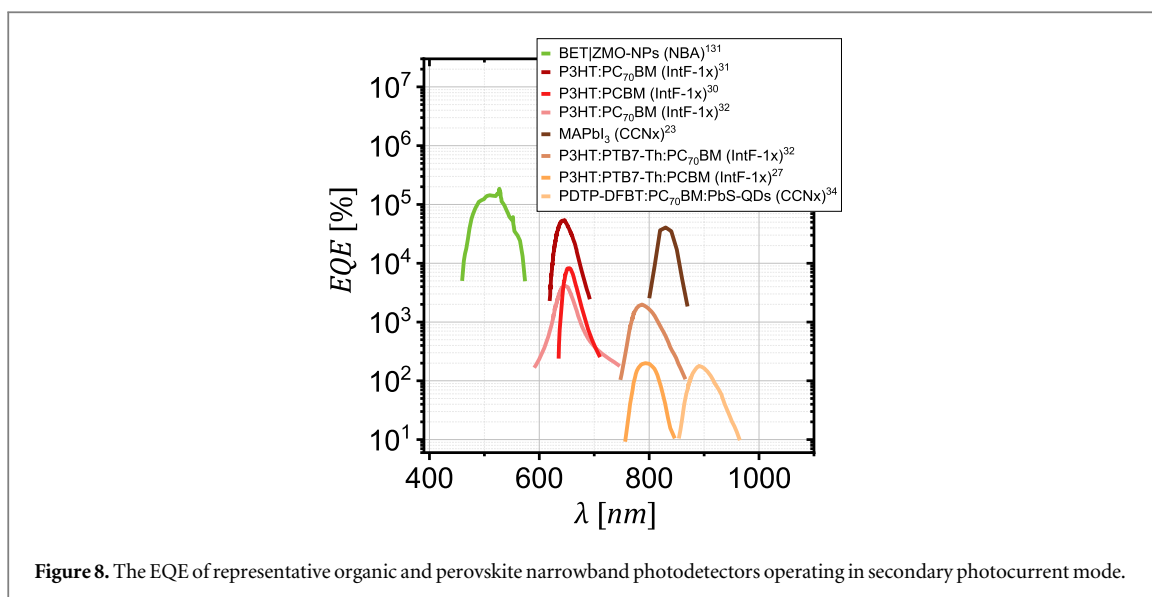


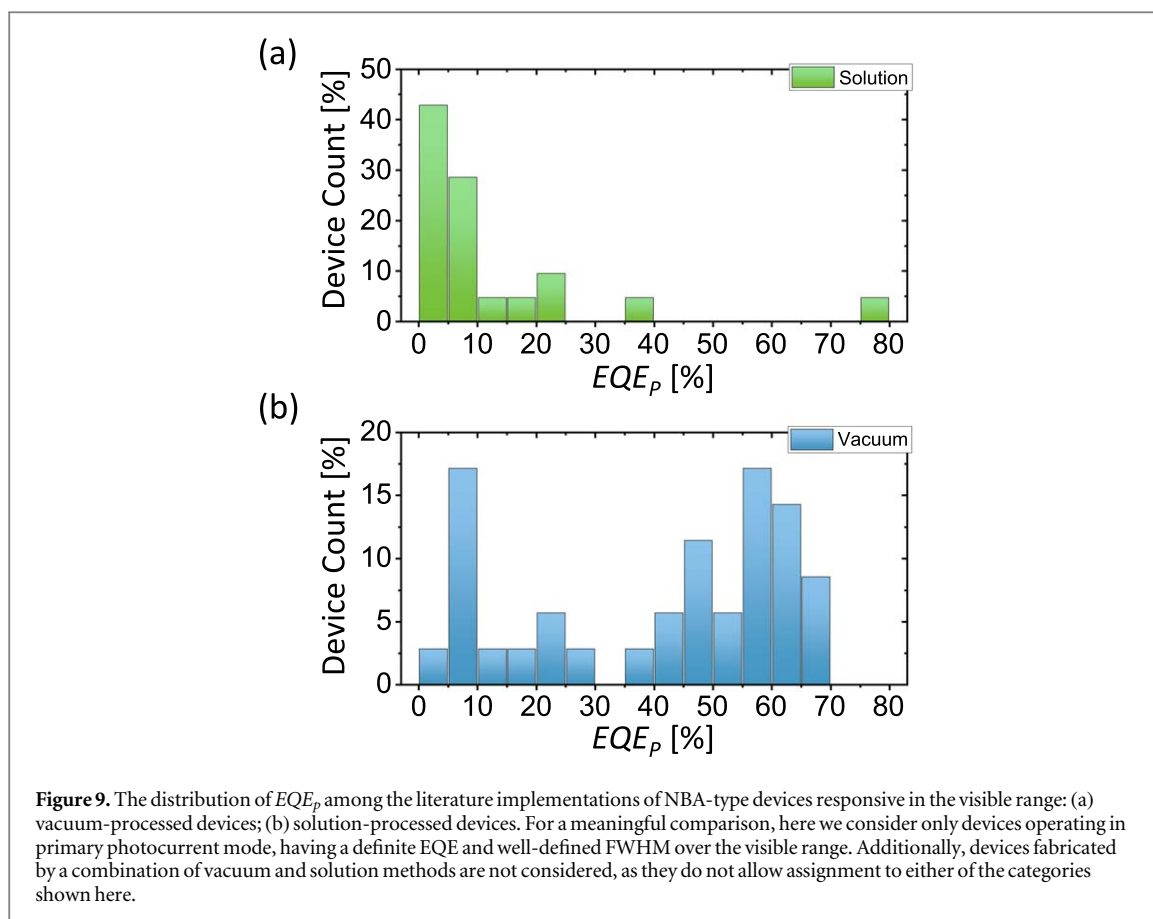
Figure 8. The EQE of representative organic and perovskite narrowband photodetectors operating in secondary photocurrent mode.

#### 6.4. Primary versus secondary photocurrent operation

While operation in primary photocurrent mode is predominant throughout the literature of narrowband organic and perovskite photodetectors, a number of works have also explored operation in secondary photocurrent mode (figure 8) [25, 27, 28, 30–34, 131]. This has been motivated by the aim of boosting phototransduction efficiency. Secondary photocurrent operation has been realised either with photoconductors [27, 28, 131] or with photodiodes under suitable bias [25, 30–34] (see section 3). In particular, the carrier trapping underlying large gains has been achieved through the inherent properties of the photoactive layer [27, 28, 131], or by incorporation of small amounts of additives serving as traps (within an organic layer) [25, 30–32, 34].

Operation in secondary photocurrent mode has enabled narrowband photodetectors with particularly large EQE figures. The BET|ZMO-NPs devices of Gao *et al* delivered an EQE of  $1.9 \cdot 10^5\%$  in the green with the NBA approach [131]. In the red, CCN devices with P3HT:PCBM: CdTe-QDs achieved an EQE of 200% [33]. IntF-1 devices based on P3HT and featuring minute amounts of PCBM or PC<sub>70</sub>BM as electron traps resulted in EQEs of about 1600% and 53 500%, respectively [30–32]. In the NIR range, CCN devices relying on PDTP-DFBT:PC<sub>70</sub>BM:PbS-QDs attained an EQE approaching 200% [34], while IntF-1 devices based on P3HT:PTB7-Th and with minute amounts of PCBM and PC<sub>70</sub>BM yielded EQE values between 200% and 2000% [25, 32]. A very large EQE ( $4 \cdot 10^4\%$ ) in the NIR range via secondary photocurrent operation has also been demonstrated with polycrystalline perovskite films [28]. As a cautionary note, while operation in secondary photocurrent mode provides very large EQEs, it generally comes with a significantly slower transient response (e.g., down to 1 Hz in some instances) [131] than operation in primary photocurrent mode. While this aspect is beyond the intended scope of this review, it is noteworthy insofar as a speed limitation may potentially inhibit the deployment of such devices for applications with critical speed requirements.

In terms of the impact of secondary photocurrent operation on spectral performance, relevant examples are provided by the studies of Shen *et al* [33, 34]. Their IntF-1 devices feature the same base photoactive materials, and operate either in primary or secondary photocurrent mode. In particular, a gain mechanism is established in the latter case by incorporation of minute amounts of additives that act as trap centres. One such work gives the same FWHM of 50 nm for both operating modes [34], while the other gives a substantially smaller FWHM (85 nm) for the device operating in primary photocurrent mode (cf. FWHM = 114 nm for the device with gain) [33]. Considering that these studies rely on the IntF-1 approach, any difference in spectral width is expected to originate from absorption differences near the onset of the photoactive material (see section 5.3) instead of the gain mechanism. While these examples are specific to the IntF-1 case, secondary photocurrent mode is not expected to directly impact the spectral behaviour for other narrowband strategies. Indeed, secondary photocurrents result from the flow of primary photocurrents [141], hence they are bound to present a closely related spectral dependence for a given photoactive layer. These examples and arguments indicate that a gain mechanism does not constitute a narrowband approach in itself, i.e., it does not generally allow a narrower spectral response than otherwise possible.



### 6.5. A processing perspective

A cross-sectional analysis of the literature reveals that important relationships hold between processing methods and narrowband photodetector performance—both for organics and perovskites—as discussed in the following. Here we specifically focus on the processing methods relevant to the photoactive materials, given their central role in determining photodetector performance. Additionally, we refer only to photodetectors operating in primary photocurrent mode, in view of the direct relationship between primary photocurrent and the inherent efficiency of the processes underlying phototransduction. Finally, for the sake of consistency, only photodetectors that are confirmed to meet the minimum spectral rejection criterion are taken into consideration.

Within the large body of organic narrowband photodetector literature, a key process-related distinction concerns whether the photoactive material is deposited via vacuum methods (e.g., thermal evaporation) or solution methods (e.g., spin coating, drop casting and inkjet printing). This dualism holds in all organic optoelectronics, where vacuum-based methods generally enable greater control over the deposition conditions, while solution-based methods are more attractive due to their greater ease and lower cost. With very few exceptions, the highest confirmed EQE values through the visible range (50%–80%) have been achieved with vacuum-deposited photoactive layers [11, 22, 46, 57–59, 61, 69–72, 120, 128, 129]. Over the same spectral range, solution-processed approaches reach beyond 50% in only one instance [95], and are around 10%–20% in most cases. An illustration of this is given in figure 9 for the literature data of NBA photodetectors responsive in the visible range. This suggests that organic vacuum-processed narrowband photodetectors (selective in the visible range) have either relied on materials with generally superior optoelectronic properties, and/or that vacuum methods enable the conditioning of such photoactive layers (e.g., via precise morphology control) towards greater optoelectronic performance. A closer inspection of the literature, however, reveals that this argument generally holds only for NBA photodetectors, which indeed constitute the largest (hence most representative) category of organic narrowband devices. Other narrowband strategies instead do not necessarily conform to this trend. For instance, all reported CCN and IntF-1 works (both with and without gain) have been conducted with solution-based methods—likely due to the large thicknesses of the photoactive layers inherently needed by these strategies, which are most conveniently achieved by solution methods. As a further example, microcavity devices (in both the visible and the NIR range) have thus far achieved their highest performance in a work employing solution methods [42], in view of its reliance on the well-conditioned CT absorption of a polymer-small

molecule blend (which can only be deposited from solution). Finally, the performance gap just mentioned for organic narrowband photodetectors in the visible range does not emerge from NIR-selective works. However, the number of NIR-selective works based on vacuum methods is too limited for one to be able to draw a conclusion within this spectral region.

While both vacuum-based and solution-based methods are both viable for perovskite deposition, it is noteworthy that the entire body of literature on narrowband perovskite photodetectors relies on photoactive layers produced via solution methods. In addition to their usual merits (ease and low cost), such reliance on solution methods arises from the widespread need of thick layers so as to achieve the optoelectronic filtering underlying narrowband photodetection with perovskites. Among the solution-based methods adopted for perovskites, a key distinction emerges between methods delivering macroscopic single crystals and the ones that result in films with varying degrees of crystallinity. Interestingly, the very few works published so far on macroscopic single-crystal narrowband perovskite photodetectors [113, 116] have not clearly manifested superior performance (in terms of EQE and  $FWHM_{EQE}$ ) with respect to the counterparts relying on films with varying degrees of crystallinity [117–119, 134] (as far as operation in primary photocurrent operation is concerned). This is in spite of the widely recognised superiority of the optoelectronic properties of perovskite single crystals (e.g., higher mobility and carrier diffusion length). While further studies are needed to clarify this aspect in relation to narrowband photodetection, it is likely that their similar performance figures at the state of the art originate from the comparable collection efficiencies realised in both types of devices to date. Indeed, single crystals (which feature generally longer carrier drift lengths  $l_c$ ) utilised for narrowband photodetectors have been produced with a significantly larger thickness  $L$ . Instead, polycrystalline layers (which generally have significantly shorter drift lengths) instead can be easily produced with smaller thicknesses. As the collection efficiency (which is a key determinant of the EQE) scales with the ratio  $l_c/L$ , it is expected that the EQE of single-crystal and polycrystalline devices will fall in the same range if the thickness is scaled accordingly. As an aside, from a technological point of view, polycrystalline layers have the added advantage of being easily scalable to large areas and generally enable higher deposition throughput.

## 7. Conclusions and outlook

This review has provided a cross-sectional view of the narrowband photodetection capabilities of organic and perovskite semiconductors. The facile tunability of the absorption properties of these two semiconductor families allows narrowband photodetection beyond the confines of conventional technologies. Firstly, narrowband organic absorbers have enabled photodetectors capable of harvesting only the photons within the spectral range of interest. This is now possible not only with great efficiency (EQE up to 50%–75% in the visible, and 30%–50% in the NIR range), but also with spectral widths  $\approx 100$  nm or less. Additionally, the refinement/emergence of strategies based on internal filtering and/or microcavity resonance has led to ultranarrowband organic and perovskite photodetectors ( $FWHM = 10$ – $50$  nm) with EQE figures up to 20%–50%, and with robust spectral rejection in many instances.

Compared to their perovskite counterpart, organic narrowband photodetectors appear to be the most mature for technological deployment. This is particularly in view of the high photoconversion efficiencies and large spectral widths that have been achieved with the (organic) narrowband-absorption approach in recent years. These figures are certainly suitable for use in colour imaging devices—e.g., for consumer electronics, but also in manifold emerging areas, such as computer vision, AI, and IoT. Ultranarrowband solutions (as achieved via microcavity-based and/or internally filtered approaches) instead see perovskites and organics as head-to-head competitors, considering that their key metrics in this area generally fall within the same range. Such performance levels already have significant potential for applications in multispectral/hyperspectral photodetection and imaging. It is apparent, however, that organics have an important edge in ultranarrowband photodetection in the NIR range, in view of their unmatched capabilities at much longer wavelengths ( $\lambda_p$  up to  $1.7 \mu\text{m}$ ) than their perovskite counterparts (highest reported  $\lambda_p$  at 850 nm). All this adds to the general advantages brought about by organic narrowband photodetectors in terms of mechanical flexibility and low-toxicity/biocompatibility, which are important requirements for a number of applications (e.g., wearables and implantable devices).

While organics have achieved very good performance, there is still plenty of room for further progress. This particularly concerns the ambitions of the narrowband absorption approach, which has the merit of having delivered the highest photoconversion efficiencies to date. On one hand, NBA photodetection with better spectral rejection is highly desirable. In this respect, the further exploration of molecular design concepts that have emerged/resurged in recent years (e.g., molecules approaching the cyanine limit, molecules capable of highly narrowband absorption via aggregation, non-fullerene acceptors) may provide valuable opportunities. On the other hand, an important challenge still holds at a processing level. Indeed, solution processing is

particularly attractive for its simplicity and potential low cost, yet solution-processed NBA-type photodetectors are lagging behind their vacuum-processed counterparts in terms of photoconversion efficiency. Therefore, it can be envisaged that further efforts to develop soluble organic compounds and solution-based processing protocols for NBA photodetectors may deliver improved performance figures and, ultimately, significant technological benefits.

Research opportunities in perovskite narrowband photodetection are also manifold. For instance, considering that perovskite narrowband photodetectors have thus far covered the NIR range only up to 850 nm, it would be highly attractive to explore new perovskite compositions that could deliver absorption onsets at longer wavelengths, so as to expand their scope to NIR spectroscopy applications. From the point of view of photoconversion efficiency, there is significant room for improvement, as EQE values of narrowband perovskite photodetectors to date have been generally inferior to their organic counterparts. This may require not only further material development to suit narrowband operation, but also device stack engineering so as to achieve more efficient charge collection within the target spectral range. In this respect, the outlook is significantly positive, considering the large EQE obtained in perovskite solar cells. The latter category of devices, however, generally relies on much thinner photoactive layers than thus far typically employed in narrowband perovskite photodetectors. Therefore, the mere adoption of thinner photoactive layers could boost the photoconversion efficiency of narrowband perovskite photodetectors, provided that recombination of photons outside the target spectral range is not key to delivering narrowband functionality. Alternatively, the further exploration of hybrid blends made of perovskites and other solution-processible semiconductors (e.g., organics) could potentially deliver high photoconversion efficiency without sacrificing narrowband functionality. Indeed, such hybrids would enable the manipulation of the absorption and carrier transport/recombination properties of perovskites, which is particularly promising in relation to internally filtered approaches. At a technological level, the challenge ahead for narrowband perovskite photodetectors arises from their complete reliance on lead-based compounds, raising significant toxicity concerns and also presenting stability issues in many of their embodiments. Therefore, it can be envisaged that the exploration of lead-free perovskites could potentially ease the technological deployment of perovskite narrowband photodetectors.

## Acknowledgments

The author acknowledges financial support from the National Natural Science Foundation of China (61750110517 and 61805166) and the Jiangsu Province Natural Science Foundation (SBK2017041510). Additionally, this work is supported by the Collaborative Innovation Center of Suzhou Nano Science & Technology, the Priority Academic Program Development of Jiangsu Higher Education Institutions (PAPD), the 111 Project, and the Joint International Research Laboratory of Carbon-Based Functional Materials and Devices.

## ORCID iDs

Vincenzo Pecunia  <https://orcid.org/0000-0003-3244-1620>

## References

- [1] Snyder W E and Qi H 2018 Introduction *Machine Vision* (Cambridge: Cambridge University Press) pp 1–7
- [2] Adan A, Alizada G, Kiraz Y, Baran Y and Nalbant A 2017 Flow cytometry: basic principles and applications *Crit. Rev. Biotechnol.* **37** 163–76
- [3] Hiltunen J *et al* 2018 Roll-to-roll fabrication of integrated PDMS–paper microfluidics for nucleic acid amplification *Lab Chip* **18** 1552–9
- [4] Ratnasingam S and Collins S 2010 Study of the photodetector characteristics of a camera for color constancy in natural scenes *J. Opt. Soc. Am. A* **27** 286
- [5] Jansen van Vuuren R *et al* 2010 Determining the absorption tolerance of single chromophore photodiodes for machine vision *Appl. Phys. Lett.* **96** 253303
- [6] Bourgeon M A *et al* 2017 «On-the-go» multispectral imaging system to characterize the development of vineyard foliage with quantitative and qualitative vegetation indices *Precis. Agric.* **18** 293–308
- [7] Rogalski A 2011 Recent progress in infrared detector technologies *Infrared Phys. Technol.* **54** 136–54
- [8] Lin H and Ying Y 2009 Theory and application of near infrared spectroscopy in assessment of fruit quality: a review *Sens. Instrum. Food Qual. Saf.* **3** 130–41
- [9] Pinti P *et al* 2018 The present and future use of functional near-infrared spectroscopy (fNIRS) for cognitive neuroscience *Ann. N. Y. Acad. Sci.* 1–25
- [10] Xu X, Davanco M, Qi X and Forrest S R 2008 Direct transfer patterning on three dimensionally deformed surfaces at micrometer resolutions and its application to hemispherical focal plane detector arrays *Org. Electron.* **9** 1122–7
- [11] Lim S J *et al* 2015 Organic-on-silicon complementary metal-oxide-semiconductor colour image sensors *Sci. Rep.* **5** 7708
- [12] Lee H-C Color image acquisition *Introduction to Color Imaging Science* 477–522 (Cambridge: Cambridge University Press)

- [13] Fossum E R 2005 Some thoughts on future digital still cameras *Image Sensors and Signal Processing for Digital Still Cameras* ed J Nakamura 305–14 (Boca Raton, FL: CRC Press)
- [14] Catrysse P B and Wandell B A 2003 Integrated color pixels in 0.18- $\mu\text{m}$  complementary metal oxide semiconductor technology *J. Opt. Soc. Am. A* **20** 2293
- [15] Kan T and Ajiki Y 2017 Silicon based mid-infrared photodetectors using plasmonic gold nano-antenna structures *TRANSDUCERS 2017-19th Int. Conf. Solid-State Sensors, Actuators Microsystems* **2** 2159–62
- [16] Sobhani A *et al* 2013 Narrowband photodetection in the near-infrared with a plasmon-induced hot electron device *Nat. Commun.* **4** 1643–6
- [17] Chen W, Kan T, Ajiki Y, Matsumoto K and Shimoyama I 2016 NIR spectrometer using a Schottky photodetector enhanced by grating-based SPR *Opt. Express* **24** 25797
- [18] Knight M W, Sobhani H, Nordlander P and Halas N J 2011 Photodetection with active optical antennas *Science* **332** 702–4
- [19] Jansen-van Vuuren R D, Armin A, Pandey A K, Burn P L and Meredith P 2016 Organic photodiodes: the future of full color detection and image sensing *Adv. Mater.* **28** 4766–802
- [20] Yoon S, Sim K M and Chung D S 2018 Prospects of colour selective organic photodiodes *J. Mater. Chem. C* **6** 13084–100
- [21] Miao J and Zhang F 2019 Recent progress on highly sensitive perovskite photodetectors *J. Mater. Chem. C* **7** 1741–91
- [22] Sakai T *et al* 2012 Doping effect of silole derivative in coumarin 30 photoconductive film *Mol. Cryst. Liq. Cryst.* **568** 74–81
- [23] Li W *et al* 2016 High-stability organic red-light photodetector for narrowband applications *Laser Photon. Rev.* **10** 473–80
- [24] Osedach T P *et al* 2012 Near-infrared photodetector consisting of J-aggregating cyanine dye and metal oxide thin films *Appl. Phys. Lett.* **101** 113303
- [25] Miao J, Zhang F, Du M, Wang W and Fang Y 2018 Photomultiplication type organic photodetectors with broadband and narrowband response ability *Adv. Opt. Mater.* **6** 1800001
- [26] Saba M, Quochi F, Mura A and Bongiovanni G 2016 Excited state properties of hybrid perovskites *Acc. Chem. Res.* **49** 166–73
- [27] Lim B T *et al* 2014 Solution-processed high-performance photodetector based on a new triisopropylsilyl ethynyl anthracene derivative *Org. Electron.* **15** 1856–61
- [28] Saidaminov M I *et al* 2016 Perovskite photodetectors operating in both narrowband and broadband regimes *Adv. Mater.* **28** 8144–9
- [29] Miao J and Zhang F 2019 Recent progress on photomultiplication type organic photodetectors *Laser Photonics Rev.* **13** 1800204
- [30] Miao J, Zhang F, Du M, Wang W and Fang Y 2017 Photomultiplication type narrowband organic photodetectors working at forward and reverse bias *Phys. Chem. Chem. Phys.* **19** 14424–30
- [31] Wang W *et al* 2017 Highly narrowband photomultiplication type organic photodetectors *Nano Lett.* **17** 1995–2002
- [32] Wang W *et al* 2018 Organic photodetectors with gain and broadband/narrowband response under top/bottom illumination conditions *Adv. Opt. Mater.* **6** 1800249
- [33] Shen L, Fang Y, Wei H, Yuan Y and Huang J 2016 A highly sensitive narrowband nanocomposite photodetector with gain *Adv. Mater.* **28** 2043–8
- [34] Shen L *et al* 2016 A filterless, visible-blind, narrow-band, and near-infrared photodetector with a gain *Nanoscale* **8** 12990–7
- [35] Vezie M S *et al* 2016 Exploring the origin of high optical absorption in conjugated polymers *Nat. Mater.* **15** 746–53
- [36] De Wolf S *et al* 2014 Organometallic halide perovskites: sharp optical absorption edge and its relation to photovoltaic performance *J. Phys. Chem. Lett.* **5** 1035–9
- [37] Hoffmann S T, Bäessler H and Köhler A 2010 What determines inhomogeneous broadening of electronic transitions in conjugated polymers? *J. Phys. Chem. B* **114** 17037–48
- [38] Marcus M, Milward J D, Köhler A and Barford W 2018 Structural information for conjugated polymers from optical modeling *J. Phys. Chem. A* **122** 3621–5
- [39] Brédas J-L, Norton J E, Cornil J and Coropceanu V 2009 Molecular understanding of organic solar cells: the challenges *Acc. Chem. Res.* **42** 1691–9
- [40] Beaujuge P M, Amb C M and Reynolds J R 2010 Spectral engineering in  $\pi$ -conjugated polymers with intramolecular donor–acceptor interactions *Acc. Chem. Res.* **43** 1396–407
- [41] Vandewal K 2016 Interfacial charge transfer states in condensed phase systems *Annu. Rev. Phys. Chem.* **67** 113–33
- [42] Tang Z *et al* 2017 Polymer: fullerene bimolecular crystals for near-infrared spectroscopic photodetectors *Adv. Mater.* **29** 1702184
- [43] Buchaca-Domingo E *et al* 2015 Direct correlation of charge transfer absorption with molecular donor:acceptor interfacial area via photothermal deflection spectroscopy *J. Am. Chem. Soc.* **137** 5256–9
- [44] Aihara S *et al* 2003 Organic photoconductive films with wavelength selectivities *2003 IEEE Workshop on CCD and Advanced Image Sensors (May 15–17, 2003, Elmau, Bavaria)*
- [45] Aihara S *et al* 2003 Wavelength selectivities of organic photoconductive films: dye-doped polysilanes and zinc phthalocyanine/tris-8-hydroxyquinoline aluminum double layer *Appl. Phys. Lett.* **82** 511–3
- [46] Seo H, Aihara S, Kubota M and Egami N 2010 Improvement in photoconductive properties of coumarin 30-vaporated film by fullerene doping for blue-sensitive photoconductors *Jpn. J. Appl. Phys.* **49** 10–3
- [47] Seo H *et al* 2011 A  $128 \times 96$  pixel stack-type color image sensor: stack of individual blue-, green-, and red-sensitive organic photoconductive films integrated with a ZnO thin film transistor readout circuit *Jpn. J. Appl. Phys.* **50** 24103
- [48] Kudo K and Moriizumi T 1981 Spectrum-controllable color sensors using organic dyes *Appl. Phys. Lett.* **39** 609–11
- [49] Fukuda T, Komoriya M, Kobayashi R, Ishimaru Y and Kamata N 2009 Wavelength-selectivity of organic photoconductive devices by solution process *Jpn. J. Appl. Phys.* **48** 04C162
- [50] Fukuda T, Kimura S, Honda Z and Kamata N 2012 Solution-processed green-sensitive organic photoconductive device using rhodamine 6g *Mol. Cryst. Liq. Cryst.* **566** 67–74
- [51] Fukuda T, Kimura S, Kamata N, Mori K and Hatano K 2013 Improved signal-to-noise ratio of green-sensitive organic photoconductive device by doping silole derivative *Mol. Cryst. Liq. Cryst.* **578** 119–26
- [52] Takada S, Ihama M and Inuiya M 2006 CMOS image sensor with organic photoconductive layer having narrow absorption band and proposal of stack type solid-state image sensors (*Sensors, Cameras, and Systems for Scientific/Industrial Applications VII*) *Proc. SPIE* **6068** 60680a–60680a-8
- [53] Sakai T, Takagi T, Hori Y and Ohtake H 2016 Light-transmissive organic photoconductive cell for stack-type image sensor *2016 IEEE Photonics Conf. (IPC)* 484–5 (Waikoloa, HI) (IEEE)
- [54] Seo H *et al* 2007 Color sensors with three vertically stacked organic photodetectors *Jpn. J. Appl. Phys.* **46** L1240–2
- [55] Aihara S *et al* 2009 Stacked image sensor with green- and red-sensitive organic photoconductive films applying zinc oxide thin-film transistors to a signal readout circuit *IEEE Trans. Electron Devices* **56** 2570–6

- [56] Seo H *et al* 2011 A  $128 \times 96$  pixel stack-type color image sensor with B-, G-, R-sensitive organic photoconductive films *Proc. 2011 Int. Image Sensor Workshop (June 8–11, 2011 Hokkaido, Japan)*
- [57] Lee K H *et al* 2013 A high performance green-sensitive organic photodiode comprising a bulk heterojunction of dimethyl-quinacridone and dicyanovinyl terthiophene *J. Mater. Chem. C* **1** 2666–71
- [58] Lee K-H *et al* 2013 Green-sensitive organic photodetectors with high sensitivity and spectral selectivity using subphthalocyanine derivatives *ACS Appl. Mater. Interfaces* **5** 13089–95
- [59] Leem D S *et al* 2013 Low dark current small molecule organic photodetectors with selective response to green light *Appl. Phys. Lett.* **103** 043305
- [60] Kim D-H *et al* 2014 A high performance semitransparent organic photodetector with green color selectivity *Appl. Phys. Lett.* **105** 213301
- [61] Lee K-H *et al* 2014 Dynamic characterization of green-sensitive organic photodetectors using nonfullerene small molecules: frequency response based on the molecular structure *J. Phys. Chem. C* **118** 13424–31
- [62] Daniel Głowacki E *et al* 2012 Intermolecular hydrogen-bonded organic semiconductors—quinacridone versus pentacene *Appl. Phys. Lett.* **101** 023305
- [63] Głowacki E D *et al* 2013 Hydrogen-bonded semiconducting pigments for air-stable field-effect transistors *Adv. Mater.* **25** 1563–9
- [64] Sakai T, Seo H, Aihara S, Kubota M and Furuta M 2013 Continuous fabrication technology for improving resolution in RGB-stacked organic image sensor *Proc. SPIE 8659, Sensors, Cameras, and Systems for Industrial and Scientific Applications XIV* 86590G
- [65] Siegmund B *et al* 2017 Organic narrowband near-infrared photodetectors based on intermolecular charge-transfer absorption *Nat. Commun.* **8** 15421
- [66] Ullbrich S, Siegmund B, Mischok A, Hofacker A and Benduhn J 2017 *Fast Organic Near-Infrared Photodetectors Based on Charge-Transfer Absorption. J. Phys. Chem. Lett.* **8** 5621–5
- [67] Iizuka M, Kudo K, Kuniyoshi S and Tanaka K 2000 Photo-spectral sensitivity controllable cells using organic multi-layer *Synth. Met.* **115** 181–3
- [68] Lamprecht B *et al* 2008 Spectrally selective organic photodiodes *Phys. Status Solidi—Rapid Res. Lett.* **2** 178–80
- [69] Higashi Y, Kim K S, Jeon H G and Ichikawa M 2010 Enhancing spectral contrast in organic red-light photodetectors based on a light-absorbing and exciton-blocking layered system *J. Appl. Phys.* **108** 034502
- [70] Sakai T, Seo H, Takagi T and Ohtake H 2016 Highly sensitive organic photoconductor using boron sub-2,3-naphthalocyanine as a red-sensitive film for stack-type image sensors *MRS Adv.* **1** 459–64
- [71] Li W *et al* 2016 Squarylium and rubrene based filterless narrowband photodetectors for an all-organic two-channel visible light communication system *Org. Electron.* **37** 346–51
- [72] Li W, Guo H, Wang Z and Dong G 2017 Narrowband organic photodiodes based on green light sensitive squarylium *J. Phys. Chem. C* **121** 15333–8
- [73] Arca F, Sramek M, Tedde S F, Lugli P and Hayden O 2013 Near-infrared organic photodiodes *IEEE J. Quantum Electron.* **49** 1016–25
- [74] Walker B J, Dorn A, Bulović V and Bawendi M G 2011 Color-selective photocurrent enhancement in coupled J-aggregate/nanowires formed in solution *Nano Lett.* **11** 2655–9
- [75] Yang Y *et al* 2011 Wavelength sensitive photodiodes in the visible based on J-type aggregated films patterned by inkjet method *Org. Electron.* **12** 405–10
- [76] Yang Y *et al* 2013 Spectral-resolving capable and integratable multilayered conductive films via an inkjet method *J. Mater. Chem. C* **1** 1739–44
- [77] Fedorov I V, Emel'yanov A V, Romashkin A V and Bobrinetskiy I I 2015 Photodetectors based on single-walled carbon nanotubes and thiamonomethinecyanine J-aggregates on flexible substrates *Semiconductors* **49** 1246–51
- [78] Fedorov I V, Romashkin A V, Emelianov A V, Nevolin V K and Bobrinetskiy I I 2017 Narrow-spectrum photosensitive structures based on J-aggregates of cyanine dyes *Semiconductors* **51** 1717–23
- [79] Liess A *et al* 2018 Ultranarrow bandwidth organic photodiodes by exchange narrowing in merocyanine H- and J-aggregate excitonic systems *Adv. Funct. Mater.* **29** 1805058
- [80] Yu G, Wang J, McElvain J and Heeger A J 1998 Large-area, full-color image sensors made with semiconducting polymers *Adv. Mater.* **10** 1431–4
- [81] Yu G *et al* 2000 Large area, full-color, digital image sensors made with semiconducting polymers *Synth. Met.* **111–112** 133–7
- [82] Wang J, Yu G, Srdanov G and Heeger A 2000 Color characterization of large area polymer image sensors *Org. Electron.* **1** 33–40
- [83] Deckman I, Lechêne P B, Pierre A and Arias A C 2018 All-printed full-color pixel organic photodiode array with a single active layer *Org. Electron.* **56** 139–45
- [84] Sim K M, Yoon S, Cho J, Jang M S and Chung D S 2018 Facile tuning the detection spectrum of organic thin film photodiode via selective exciton activation *ACS Appl. Mater. Interfaces* **10** 8405–10
- [85] Kim S K, Park S, Son H J and Chung D S 2018 Synthetic approach to achieve a thin-film red-selective polymer photodiode: difluorobenzothiadiazole-based donor-acceptor polymer with enhanced space charge carriers *Macromolecules* **51** 8241–7
- [86] Zhong Y *et al* 2017 Helical nanoribbons for ultra-narrowband photodetectors *J. Am. Chem. Soc.* **139** 5644–7
- [87] Yu Y *et al* 2016 A perylene bisimide derivative with a LUMO level of  $-4.56$  eV for non-fullerene solar cells *J. Mater. Chem. C* **4** 4134–7
- [88] Kozma E and Catellani M 2013 Perylene diimides based materials for organic solar cells *Dye. Pigment.* **98** 160–79
- [89] Chen R-F *et al* 2006 Fluorene and silafluorene conjugated copolymer: a new blue light-emitting polymer *Synth. Met.* **156** 1161–7
- [90] Kobayashi R *et al* 2010 Improved photoconductive characteristics of solution-processed organic device by doping silole derivative *Mol. Cryst. Liq. Cryst.* **519** 206–12
- [91] Yoon S, Ha J, Cho J and Chung D S 2016 Nonabsorbing acceptor-based planar heterojunction for color-selective and high-detectivity polymer photodiodes *Adv. Opt. Mater.* **4** 1933–8
- [92] Fukuda T, Kimura S, Honda Z and Kamata N 2011 Blue-sensitive organic photoconductive device with MDMO-PPV doped F8BT layer *Mol. Cryst. Liq. Cryst.* **539** 542–9
- [93] Fukuda T *et al* 2010 Improvements in photoconductive characteristics of organic device using silole derivative *Jpn. J. Appl. Phys.* **49** 01AC05
- [94] Fukuda T, Suzuki T, Kobayashi R, Honda Z and Kamata N 2009 Organic photoconductive device fabricated by electrospray deposition method *Thin Solid Films* **518** 575–8
- [95] Sato Y, Kajii H and Ohmori Y 2014 Improved performance of polymer photodetectors using indium–tin-oxide modified by phosphonic acid-based self-assembled monolayer treatment *Org. Electron.* **15** 1753–8
- [96] Antognazza M R, Musitelli D, Perissinotto S and Lanzani G 2010 Spectrally selected photodiodes for colorimetric application *Org. Electron.* **11** 357–62

- [97] Antognazza M R, Scherf U, Monti P and Lanzani G 2007 Organic-based tristimuli colorimeter *Appl. Phys. Lett.* **90** 163509
- [98] Armin A, Jansen-van Vuuren R D, Kopidakis N, Burn P L and Meredith P 2015 Narrowband light detection via internal quantum efficiency manipulation of organic photodiodes *Nat. Commun.* **6** 6343
- [99] Blouin N *et al* 2008 Toward a rational design of poly(2,7-Carbazole) derivatives for solar cells *J. Am. Chem. Soc.* **130** 732–42
- [100] Zhang G, Fu Y, Xie Z and Zhang Q 2011 Synthesis of low bandgap polymer based on 3,6-dithien-2-yl-2,5-dialkylpyrrolo[3,4-c]pyrrole-1,4-dione for photovoltaic applications *Sol. Energy Mater. Sol. Cells* **95** 1168–73
- [101] Sadhanala A *et al* 2014 Preparation of single-phase films of  $\text{CH}_3\text{NH}_3\text{Pb}(\text{I}_{1-x}\text{Br}_x)_3$  with sharp optical band edges *J. Phys. Chem. Lett.* **5** 2501–5
- [102] Miyata A *et al* 2015 Direct measurement of the exciton binding energy and effective masses for charge carriers in organic-inorganic tri-halide perovskites *Nat. Phys.* **11** 582–7
- [103] D’Innocenzo V *et al* 2014 Excitons versus free charges in organo-lead tri-halide perovskites *Nat. Commun.* **5** 3586
- [104] Comin R *et al* 2015 Structural, optical, and electronic studies of wide-bandgap lead halide perovskites *J. Mater. Chem. C* **3** 8839–43
- [105] Senanayak S P *et al* 2017 Understanding charge transport in lead iodide perovskite thin-film field-effect transistors *Sci. Adv.* **3** e1601935
- [106] Nazarenko O, Yakunin S, Morad V, Cherniukh I and Kovalenko M V 2017 Single crystals of caesium formamidinium lead halide perovskites: solution growth and gamma dosimetry *NPG Asia Mater.* **9** e373–373
- [107] Hu X *et al* 2018 Visualizing carrier transport in metal halide perovskite nanoplates via electric field modulated photoluminescence imaging *Nano Lett.* **18** 3024–31
- [108] Yang J and Kelly T L 2017 Decomposition and cell failure mechanisms in lead halide perovskite solar cells *Inorg. Chem.* **56** 92–101
- [109] Noh J H, Im S H, Heo J H, Mandal T N and Seok S I L 2013 Chemical management for colorful, efficient, and stable inorganic–organic hybrid nanostructured solar cells *Nano Lett.* **13** 1764–9
- [110] Seo H, Sakai T, Ohtake H and Furuta M 2014 Stacked organic photoconductive films and thin-film transistor circuits separated by thin silicon nitride for a color image sensor *IEEE SENSORS 2014 Proc. (Valencia, Spain)* 1672–5 (IEEE)
- [111] Sakai T *et al* 2015 Color image sensor with organic photoconductive films *2015 IEEE Int. Electron Devices Meeting (IEDM) Washington, DC* 30.3.1–30.3.4 (IEEE)
- [112] Takagi T, Seo H, Sakai T, Ohtake H and Furuta M 2016 Image sensor with organic photoconductive films by stacking red/green and blue components *Electron. Imaging* **2016** 1–4
- [113] Yakunin S, Shynkarenko Y, Dirin D N, Cherniukh I and Kovalenko M V 2017 Non-dissipative internal optical filtering with solution-grown perovskite single crystals for full-colour imaging *NPG Asia Mater.* **9** e431
- [114] Lyons D M *et al* 2014 Narrow band green organic photodiodes for imaging *Org. Electron.* **15** 2903–11
- [115] Chen E-C *et al* 2010 Polymer photodetector with voltage-adjustable photocurrent spectrum *Appl. Phys. Lett.* **96** 43507
- [116] Fang Y, Dong Q, Shao Y, Yuan Y and Huang J 2015 Highly narrowband perovskite single-crystal photodetectors enabled by surface-charge recombination *Nat. Photonics* **9** 679–86
- [117] Lin Q, Armin A, Burn P L and Meredith P 2015 Filterless narrowband visible photodetectors *Nat. Photonics* **9** 687–94
- [118] Rao H, Li W, Chen B, Kuang D and Su C 2017 *In Situ* Growth of 120 cm<sup>2</sup>  $\text{CH}_3\text{NH}_3\text{PbBr}_3$  Perovskite Crystal Film on FTO Glass for Narrowband-Photodetector *Adv. Mater.* **29** 1602639
- [119] Wu Y, Li X, Wei Y, Gu Y and Zeng H 2018 Perovskite photodetectors with both visible-infrared dual-mode response and super-narrowband characteristics towards photo-communication encryption application *Nanoscale* **10** 359–65
- [120] Bulliard X *et al* 2016 Dipolar donor–acceptor molecules in the cyanine limit for high efficiency green-light-selective organic photodiodes *J. Mater. Chem. C* **4** 1117–25
- [121] Fukuda T *et al* 2012 Improved optical-to-electrical conversion efficiency by doping silole derivative with low ionization potential *Phys. Status Solidi Appl. Mater. Sci.* **209** 2324–9
- [122] Kimura S *et al* 2012 Doping effect of ethylcarbazole-contained-silole in blue-sensitive organic photoconductive device *Mol. Cryst. Liq. Cryst.* **566** 54–60
- [123] Pandey A K, Johnstone K D, Burn P L and Samuel I D W 2014 Sensors and actuators B: chemical solution-processed pentathiophene dendrimer based photodetectors for digital cameras *Sensors Actuators B. Chem.* **196** 245–51
- [124] Yoon S, Ha Y-H, Kwon S-K, Kim Y-H and Chung D S 2018 Fabrication of high performance, narrowband blue-selective polymer photodiodes with dialkoxynaphthalene-based conjugated polymer *ACS Photonics* **5** 636–41
- [125] Jansen-van Vuuren R D, Pivrikas A, Pandey A K and Burn P L 2013 Colour selective organic photodetectors utilizing ketocyanine-cored dendrimers *J. Mater. Chem. C* **1** 3532
- [126] Han M G *et al* 2016 Narrow-band organic photodiodes for high-resolution imaging *ACS Appl. Mater. Interfaces* **8** 26143–51
- [127] Sung M J, Yoon S, Kwon S-K, Kim Y-H and Chung D S 2016 Synthesis of phenanthro[1,10,9,8-cdefg]carbazole-based conjugated polymers for green-selective organic photodiodes *ACS Appl. Mater. Interfaces* **8** 31172–8
- [128] Heo S *et al* 2017 Device performance enhancement via a Si-rich silicon oxynitride buffer layer for the organic photodetecting device *Sci. Rep.* **7** 1516
- [129] Satoh R *et al* 2017 Bi-layered metal-oxide thin films processed at low-temperature for the encapsulation of highly stable organic photo-diode *Org. Electron.* **41** 259–65
- [130] Sung M J, Kim K, Kwon S, Kim Y and Chung D S 2017 Phenanthro[110,9,8-cdefg]carbazole-thiophene, donor–donor copolymer for narrow band green-selective organic photodiode *J. Phys. Chem. C* **121** 15931–6
- [131] Gao L *et al* 2017 Flexible filter-free narrowband photodetector with high gain and customized responsive spectrum *Adv. Funct. Mater.* **27** 1702360
- [132] Zhang H *et al* 2015 Transparent organic photodetector using a near-infrared absorbing cyanine dye *Sci. Rep.* **5** 9439
- [133] Ihama M *et al* 2011 CMOS image sensor with an overlaid organic photoelectric conversion layer: optical advantages of capturing slanting rays of light *Proc. 2011 Int. Image Sensor Workshop (June 8–11, 2011 Hokkaido)* P33
- [134] Li L *et al* 2017 Self-Filtered Narrowband Perovskite Photodetectors with Ultrafast and Tuned Spectral Response *Advanced Optical Materials* **5** 1700672
- [135] Yoon S, Koh C W, Woo H Y and Chung D S 2018 Systematic optical design of constituting layers to realize high-performance red-selective thin-film organic photodiodes *Adv. Opt. Mater.* **6** 1701085
- [136] Lupton J M *et al* 2003 Organic microcavity photodiodes *Adv. Mater.* **15** 1471–4
- [137] An K H, O’Connor B, Pipe K P and Shtein M 2009 Organic photodetector with spectral response tunable across the visible spectrum by means of internal optical microcavity *Org. Electron.* **10** 1152–7

- [138] Koeppe R *et al* 2003 One- and two-photon photocurrents from tunable organic microcavity photodiodes *Appl. Phys. Lett.* **82** 2601–3
- [139] Ullbrich S *et al* 2017 Fast organic near-infrared photodetectors based on charge-transfer absorption *J. Phys. Chem. Lett.* **8** 5621–5
- [140] Ihama M *et al* 2010 Proposal of new organic CMOS image sensor for reduction in pixel size *Fujifilm Research Development* **55–2010** 14–7
- [141] Bube R H 1960 *Photoconductivity of Solids* (New York: Wiley)